Optimal Operation and Design of Solar-Thermal Energy Storage Systems

by

Enrique Lizarraga-García

Ingeniero Industrial, Universidad Pública de Navarra (2009)

Submitted to the Department of Mechanical Engineering
in partial fulfillment of the requirements for the degree of

Master of Science in Mechanical Engineering

at the

MASSACHUSETTS INSTITUTE OF TECHNOLOGY

June 2012

Author .....
Department of Mechanical Engineering
May 24, 2012

Certified by .....
Alexander Mitsos
Rockwell International Assistant Professor
Thesis Supervisor

Accepted by .....
David E. Hardt
Ralph E. and Eloise F. Cross Professor of Mechanical Engineering
Chairman, Committee on Graduate Students

Optimal Operation and Design of Solar-Thermal Energy Storage Systems

by

Enrique Lizarraga-García

Submitted to the Department of Mechanical Engineering
on May 24, 2012, in partial fulfillment of the
requirements for the degree of
Master of Science in Mechanical Engineering

Abstract

The present thesis focuses on the optimal operation and design of solar-thermal energy storage systems.

First, optimization of time-variable operation to maximize revenue through selling and purchasing electricity to/from the grid is presented for a thermal energy storage system. Time-variable electricity prices and electricity buy-back from the grid to re-charge the energy storage is considered. The concentrated solar power on demand (CSPonD) concept, in which a salt pond receives solar energy, stores thermal energy, and delivers thermal energy to the power cycle is considered. Electric heaters are added to the CSPonD concept, allowing for periods of electricity buy-back from the grid to re-charge the energy storage. System-level models are developed and optimization of the design and operation is performed with local solvers. Three main case studies are considered: the first case study investigates the optimization of time-variable operation without electrical heating under time-invariant electricity price; the second case study optimizes the operation under time-variant electricity price without electric heaters; the third case study optimizes the operation under time-variant electricity price allowing charging of the pond using the grid electricity. The first case study reflects the time-invariant tariff model, whereas the second and third case studies consider a time-of-use feed-in-tariff. Two hourly price profiles are considered in order to assess the influence of it on the optimal design and operation of the thermal energy storage. The first electricity profile consists of a price profile that fluctuates moderately, and the second price profile fluctuates highly, including negative prices. The results show significant increase in the revenue when adding electric heaters. Under the moderately fluctuating electricity price, the use of heaters increases the revenue significantly, compared to the same case with no electric heaters considered. Under the highly fluctuating electricity price, the use of heaters more than doubles the revenue, compared to the same case with no electric heaters considered.

Also, the performance analysis of a regenerative thermal energy storage system with enhancement heat transfer structures is presented. In a regenerative thermal storage system,

thermal energy is transferred from a hot heat transfer fluid to the storage unit core elements during charge, and from the core elements to the cold heat transfer fluid during discharge. Herein, concrete as the solid storage material, nitrate solar salt as the heat transfer fluid, and aluminum plates as the heat transfer structures is considered. The discharge process from uniform initial temperature is studied with different configurations (pure concrete and concrete enhanced by transfer structures), operation strategies (laminar versus turbulent flow regimes), and dimensions. Results show a significant decrease in the cost of the thermal energy storage system when heat transfer structures are added, as well as a better performance in terms of discharge efficiency and discharge time period. The amount of solar salt needed for this configuration is approximately one fourth that required for a nitrate two-tank system operating with the same temperature difference.

Thesis Supervisor: Alexander Mitsos
Title: Rockwell International Assistant Professor

Acknowledgments

I am very grateful for the advice and support of Prof. Alexander Mitsos, for his guidance and for providing me an opportunity to grow as a person, student and engineer. I would like to express my gratitude to Dr. Amin Ghobeity and Mark Totten for their colaboration. Also, the comments given by Dr. Annelies Vandersickel have greatly improved and clarified this work.

I would like thank my labmates during these two years at MIT. Dan Williams, Tawfiq Dahdah, Surekha Gunasekaran, Elysia Sheu, Gina Zak, Hussam Zebian, Corey Noone, Chris Williams, Nick Mancini, Abhishek Bajpayee, Angelos Tsoukalas, Hadi Ghasemi, Jun Fu, and Ragheb El Khaja, with whom I have grown. Our conversations have greatly influenced this thesis.

Most importantly, I would like to thank all my friends, here and back home, who helped me get through these intense two years. Specially, to the people that get together every weekend at the headquarters. To the Greek basketball team, specially the captain, that let me remember the good old times. To my flatmates, Owen, Yiquing, Roberto, Jordi, Eugene and Laura. To Tugores and Gomà. To my parents and family.

Finally, I am greatly thankful to my postgraduate fellowship from the foundation Obra Social "la Caixa".

THIS PAGE INTENTIONALLY LEFT BLANK

Contents

List of Figures

List of Tables

Chapter 1

Introduction

Concentrated Solar Power (CSP) offers a clean alternative to traditional electricity sources. However, electricity demand and solar insulation curves do not always match. This feature is observed in Figures 1-1 to 1-3, where the Direct Normal Radiation (DNI) [43], the electricity price [46], and the electricity demand [54] for January 14^{th}, April 15^{th} and July 30^{th} 2011, respectively, in Seville, Spain, is shown.

One of the key concerns with the use of renewable energy sources (RES) in general, and CSP in particular, to produce electricity at a large scale are the low capacity factor, defined as the ratio of the actual output of a power plant over a period of time and its potential output if it had operated at full nominal capacity the entire time. In CSP, its low capacity factor comes from the inherent intermittent nature of the high temperature source, the sun light, with variability in at least three time scales (seasonal, hourly and weather-related). Another key concern is the high levelized cost of electricity (LCOE). Inclusion of energy storage with RES may increase the capacity factor and decrease LCOE. However, when comparing different RES technologies with and without energy storage, LCOE is not a suitable metric since it ignores dispatchability and the time of day (TOD) the electricity is generated, two of the key characteristics for asset generation [51]. The objective of the thermal energy storage system inclusion is to match the electricity demand curve, and produce electricity during no-sun periods where the electricity price is higher than during the periods when sun

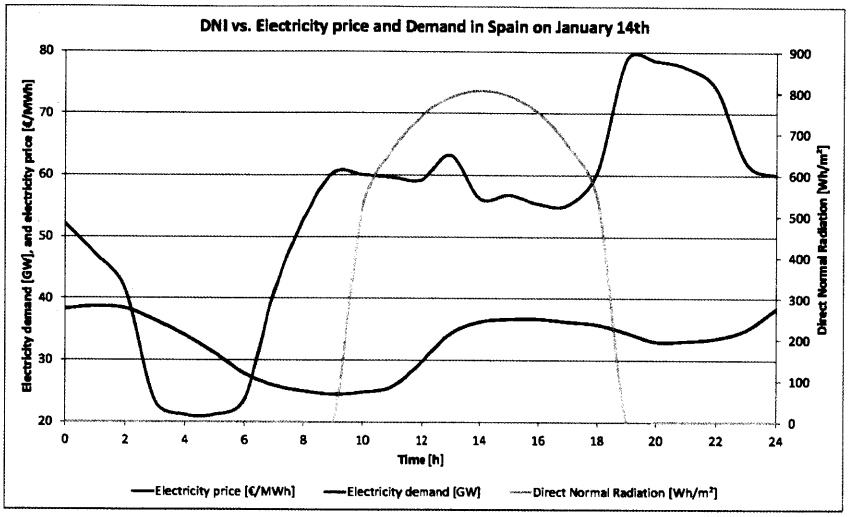

Figure 1-1: Direct Normal Radiation (DNI) [43], the electricity price [46], and the electricity demand [54] for January 14^{th} 2011 in Seville, Spain

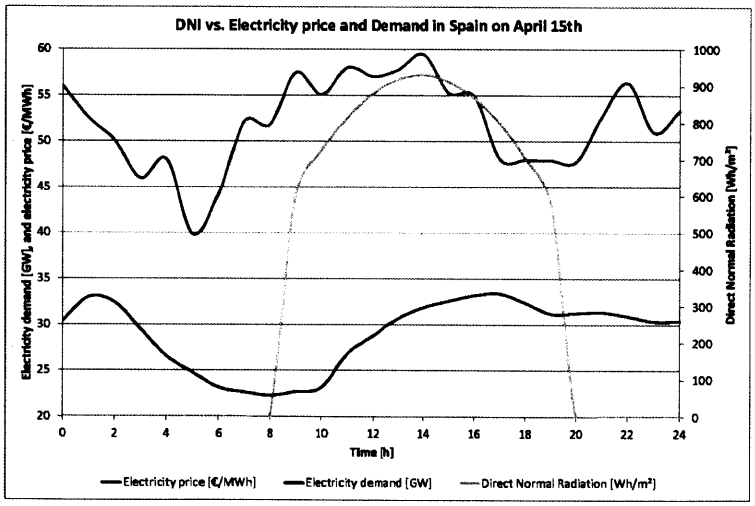

Figure 1-2: Direct Normal Radiation (DNI) [43], the electricity price [46], and the electricity demand [54] for April 15^{th} 2011 in Seville, Spain

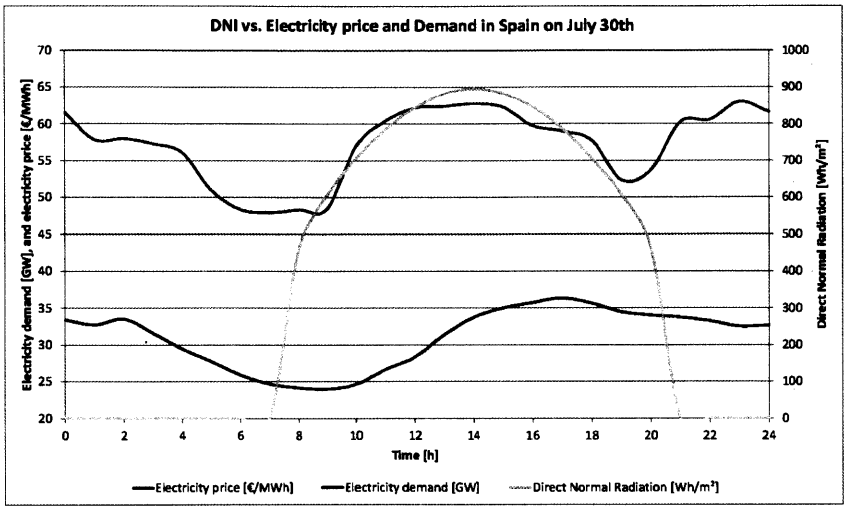

Figure 1-3: Direct Normal Radiation (DNI) [43], the electricity price [46], and the electricity demand [54] for July 30^{th} 2011 in Seville, Spain

is shining. For example, in Figure 1-3, it might be more profitable to produce electricity from 10 pm to 12 am, than in the periods from 8 to 10 am, and 6 to 8 pm, even though the solar-thermal power plant is not receiving solar radiation at that time.

Since energy storage us important, two studies are considered herein. In Chapter 2, optimal operation of a solar-thermal power plant with thermal energy storage and electricity buy-back from the grid is presented. Revenue maximization through selling and purchasing electricity to/from the grid is sought. The concentrated solar power on demand (CSPonD) concept, in which a salt pond receives solar energy, stores thermal energy, and delivers thermal energy to the power cycle is considered.

In Chapter 3, a mixture of solid and liquid thermal energy storage system is analyzed. Therein, the effect of enhancement heat transfer structures on the performance of a regenerative thermal energy storage system is analyzed. Concrete as the solid storage material, nitrate solar salt as the heat transfer fluid, and aluminum plates as the heat transfer structures are considered.

THIS PAGE INTENTIONALLY LEFT BLANK

Chapter 2

Optimal Operation of a Solar-Thermal Power Plant with Thermal Energy Storage and Electricity Buy-Back from Grid

2.1 Introduction

Two key concerns with the use of renewable energy sources (RES) to produce electricity at a large scale are the low reliability and high levelized cost of electricity (LCOE). Inclusion of energy storage with RES may increase reliability and decrease LCOE. However, when comparing different RES technologies with and without energy storage, LCOE is not a suitable metric since it ignores dispatchability and the time of day (TOD) the electricity is generated, two of the key characteristics for asset generation [51]. E.g., photovoltaics (PV) without tracking versus concentrated solar power (CSP) with storage, lower LCOE does not imply higher revenue. Thus, time-variable production of renewable electricity systems is an important issue as both the energy source and the electricity demand are time-variable. This article addresses some key questions with respect to the time-variable operation of renewable

systems. First and foremost, *is time-variable operation of renewable energy systems feasible?* Assuming so, *can a renewable system be operated in an on-demand way? Will time-variable operation result in an appreciable increase in revenue, or the ability to meet a time-variable demand and the peak electricity load? Is it economic to purchase electricity back from the grid at times of low prices and use it to recharge the storage?* System-level models and nonlinear programming (NLP) with dynamics embedded is used to optimize the revenue of a solar-thermal energy system under alternative simulated market conditions. Optimization of operation is considered in the field of conventional power producers [10, 49, 75]. In solar-thermal power plants, operation strategies have been employed to increase the average thermal efficiency [13, 22, 55] and also to maximize revenue under a fixed plant design, so that the power plant is consequently run with a price-driven strategy [74]. Therein, a methodology based on electricity pricing and weather forecasting is shown on how to set up an economically optimized bidding strategy at the energy exchange, which takes the solar resource and the price information into account.

There are a number of thermal energy concepts tested in solar energy plants around the world. Two-tank system with molten salt mixtures [2, 18, 20, 47] is among the most developed and tested concepts. Although the collector cost is the single largest cost of solar-thermal plants, the additional cost of two-tank thermal energy storage system is significant. As such, alternative designs such as thermocline and rafted thermocline [19, 73] have been investigated. Herein the concentrated solar power on demand (CSPonD) concept is considered, an integrated volumetric solar energy receiver and thermal storage system proposed by Slocum et al. [60].

The use of CSPonD for cogeneration concepts (e.g., power production and water desalination) was investigated in [17, 16]. Therein, systematic optimization predominantly of design and constant power generation strategies was considered. Herein, optimization of time-variable operation is considered for electricity generation that uses the solar energy collected by CSPonD. More specifically, the main purpose of the present study is to assess the potential of a solar-thermal generation system considering fluctuating electricity prices.

The nominal power output is 35 MWe, with a thermal energy storage capacity of 15 hours. In addition, the usage of 20 MW electric heaters to charge the thermal energy storage when electricity prices are negative or sufficiently low, i.e., purchasing back the electricity from the grid is considered. Negative electricity prices have occurred recently in many places including Germany, for instance, with prices as low as −0.5 €/kWh [41], or in West Texas where the real time price of electricity was negative for 23% of April 2009 [31]. Herein, two electricity profiles are considered. The first one is a fictitious electricity price distribution that fluctuates moderately. The second price profile fluctuates highly, including negative electricity prices, and is obtained from the actual electricity prices on the 22^{nd} of April 2009 in West Texas [52]. The day chosen is by no means an average day; however, there are days of more fluctuating electricity prices including days with negative average price.

2.2 System Description and Models

A system-level schematic of the design considered herein is shown in Fig. 2-1. The heat withdrawn from the CSPonD is used in the steam generator of a steam cycle. The models calculate the time-variable operating conditions including solar energy input to the system, salt temperature within the cold and hot tanks, and the heat transfer rates between various components of the design (e.g., tank walls, the lid, the moving thermal barrier, etc.) via radiation and conduction. Decision variables, described in Section 2.4, are calculated by the optimizer.

The models are based largely on [17, 16, 15], with modifications to include electric heaters. The steam cycle is not modeled herein, and instead a constant power block efficiency of 0.35 is assumed. This is a substantial approximation; however, it is noteworthy that the isentropic efficiency of some turbines with regulation stage added is found to be approximately constant for a part load of more than ~50% [69].

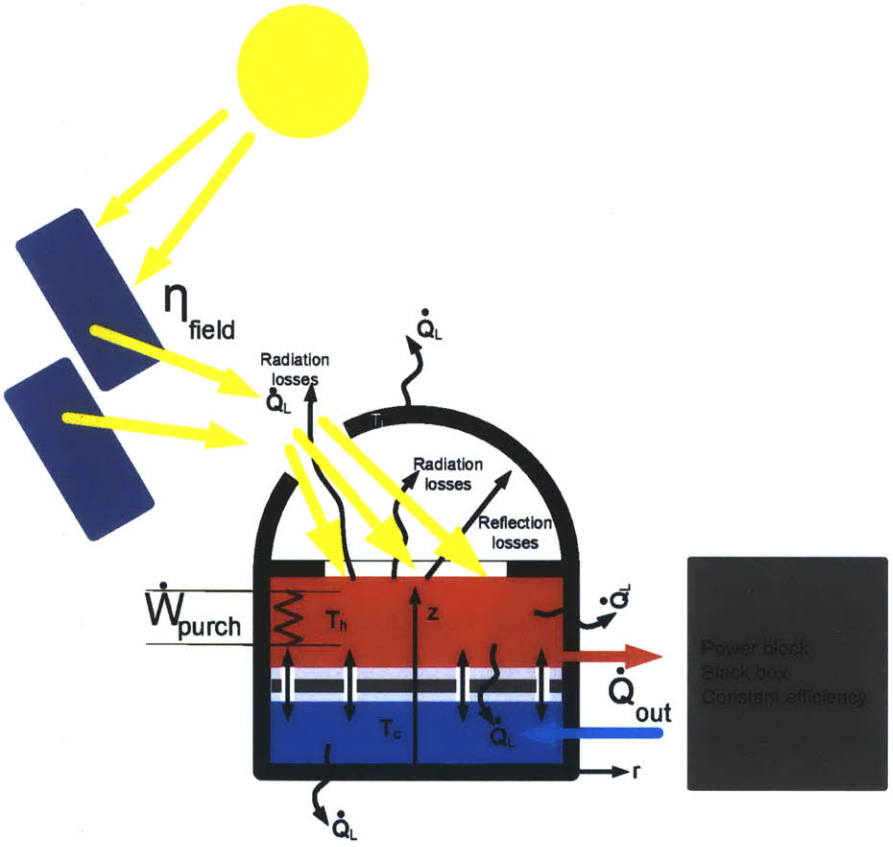

Figure 2-1: Physical models of the solar-thermal power plant: radiation model, heliostat field model, and virtual two-tank model

2.3 Computational Infrastructure

The physical model is written in JACOBIAN (v4.0) [44], and optimal operation is obtained employing the simultaneous method of dynamic optimization using collocation [3] with GAMS (v23.7.3 and v23.8) [4] as the modeling system and IPOPT [72] as the local solver. The model is automatically translated from JACOBIAN to GAMS with an in-house code. Additionally, the sequential method [3] using control vector parameterization is employed with IPOPT as the local solver, and JACOBIAN as the simulator. To overcome nonconvexity, heuristic global optimization is performed in the sequential approach via multistart in a parallel computing environment. Moreover, the sequential method is used to obtain the start-up and shutdown optimized values, which are taken fixed in the simultaneous approach.

In the simultaneous method, full discretization of the differential algebraic equations (DAEs) is implemented. Considering a multi-period dynamic optimization problem, each period is represented by finite time elements, and state and control variables are represented by piecewise polynomials in each of the elements. This results in a large NLP without an embedded DAE solver. This approach is suitable for problems with a large number of degrees of freedom. Differential and algebraic equations are solved at selected points in time, which is discretized in two levels. The main discretization gives the main finite time elements. Their length, h_i, i=1,...,L, can be different from each other. Within each finite element, state and control variables are represented based on Lagrange interpolation polynomials of order K+1. The choice of the K+1 interpolation points, τ_k, k=0,...,K, the second level of time discretization, is made following the suggestion of [3]. These polynomials belong to the Gauss-Jacobi class. Herein, these points are the roots of Gauss-Radau polynomial of degree K=3. The control profiles are enforced to be piecewise constant within the main finite time elements. In this case, the start-up/shutdown times are not decision variables, since their values are needed to calculate the radiation input. As a consequence, their values are fixed, and come from the sequential approach results. The number of main finite elements, L, for each case study is shown in Table 2.1. The case studies listed in the table are described in the following section.

Table 2.1: Number of main finite time elements, L, of each case study

Case study	**L**
Constant moderately fluctuating price	36
Variable moderately fluctuating price	26
Electrical heating moderately fluctuating price	34
Constant highly fluctuating price	36
Variable highly fluctuating price	31
Electrical heating highly fluctuating price	40

2.4 Optimal Operation of CSPonD

Optimal operation of the virtual two-tank for a day is investigated in this section, considering several conditions including electrical heating of the hot part of the tank. For the heaters, a total of 20 MW electric heating power is considered. To reach it, a set of small scale high temperature Hopper heaters of 4.032 kW power could be added, with a capital cost of 180 $ each [70]. These heaters would be attached to the wall. With a wattage per unit area of 10 W/in^2, a total surface area of approximately 1,290 m^2 is needed. Considering the pond diameter is 25 m, and the interference with the moving thermal barrier in the hot/cold salt separation, the best way to reach this area would be adding internal vertical walls in the hot tank, hanging from the roof of the tank. Moreover, this feature would help to distribute the heat more uniformly. In order to implement this, salt is always required in the hot side. Herein, the smallest height of hot salt reached is 5.7 m, enough to allow the *electrical heating* design.

2.4.1 Case Studies

Previous optimization studies on CSPonD [17, 16] have focused on optimal operation, assuming a constant power generation and electricity price. The present work focuses on optimizing the operation considering economical parameters, including hourly fluctuations of the price, if any. More specifically, the main goals are investigating the feasibility and optimality of a time-variable operation for the concept described in Section 2.1 (Fig. 2-1).

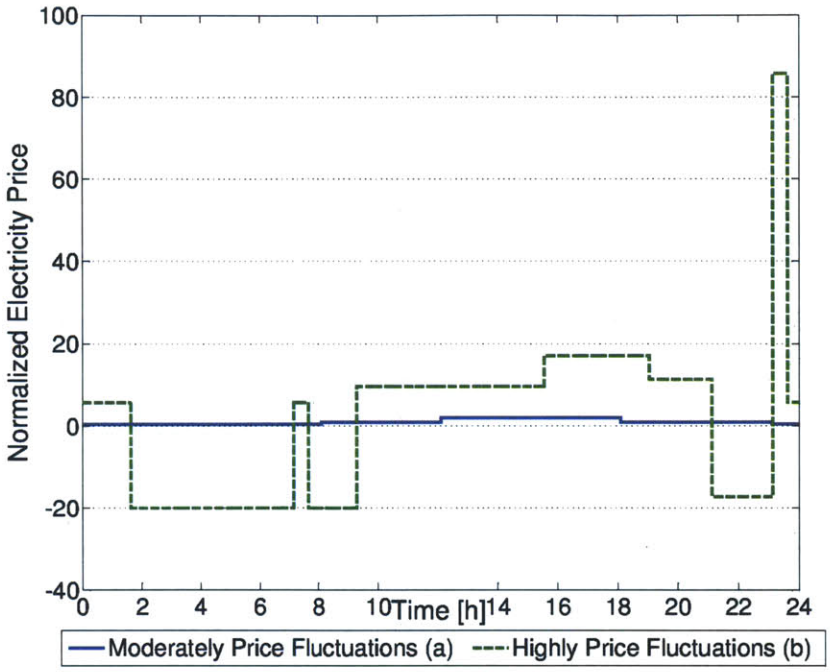

Figure 2-2: Normalized electricity price profiles used herein: solid blue line shows the moderately fluctuating price profile (case a); dashed green line shows the highly fluctuating price profile, including negative electricity prices (case b)

Three main case studies are considered:

- *Constant price* considers variable operation under average electricity price
- *Variable price* considers variable operation under time-variable electricity price
- *Electrical heating* considers variable operation with electric heaters included in the pond under time-variable electricity price

Two hourly electricity price distributions are considered for the case studies *constant price*, *variable price*, *electrical heating*: (a) Moderately fluctuating electricity price. (b) Highly fluctuating electricity price. Fig. 2-2 shows the normalized electricity price profiles used, that is, the electricity price profile divided by its respective average value over the day. Hence, a total of six case studies is considered in the following.

Figure 2-3: Optimization variables

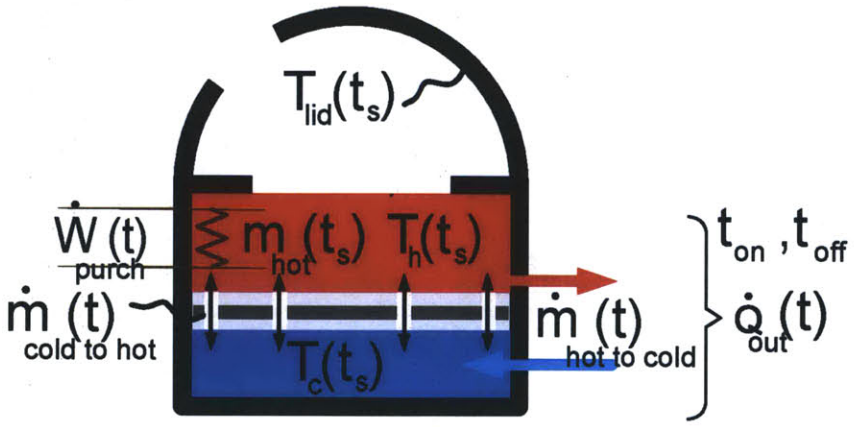

Constant price case study uses time-weighted averaged prices, $\hat{c}$, found from:

$$\hat{c} = \frac{1}{24} \int_0^{24h} c(t)dt. \tag{2.1}$$

The constant electricity price, $\hat{c}$, found from the time-weighted averaged of the electricity price profiles (a) and (b) are equal to 0.260 \$/kWh and 0.00175 \$/kWh, respectively.

2.4.2 Optimization Variables and Objectives

Optimization Variables

The optimization variables and their bounds are shown in Table 2.3, and Figure 2-3. These are the initial temperatures of the hot tank, the cold tank, and the lid, the initial mass of salt in the hot tank, the mass flow rate from the hot tank to the cold tank, the mass flow rate from the cold tank to the hot tank, the heat transfer rate out from the lid, and the electricity purchased from the grid (only for the case study of electric heaters). The initial time is the sunrise time, t_s. Additionally, the optimal start-up and shutdown time values are obtained in the sequential method, and kept fixed in the simultaneous approach.

Objectives

The objective of the optimization in all six case studies considered is maximizing the revenue over 24 hours of continuous operation. The objective function in its most general form is:

$$Obj(c(t), \dot{Q}_{output}(t), \dot{W}_{purchased}(t)) = \int_{t_s}^{t_s+24h} c(t)\cdot\{\dot{Q}_{output}(t)\cdot\eta_{power} - \dot{W}_{purchased}(t)\}\cdot dt \quad (2.2)$$

where $c(t)$ is the electricity price at time t, $\dot{Q}_{output}(t)$ is the total heat transfer rate out of the thermal storage system at time t, η_{power} is the power block efficiency, and $\dot{W}_{purchased}(t)$ is the electric power purchased from the grid to run the electric heaters at time t. Clearly, some of the terms in the objective function are set to zero or a constant value depending on the conditions considered in the case study, e.g., for case studies *constant price* and *variable price*, $\dot{W}_{purchased}(t) = 0$. Moreover, for case studies *constant price*, the corresponding $\hat{c}$ is used for $c(t)$ in the objective function.

The total heat transfer rate out of the thermal storage system and, thus, into the power cycle $\dot{Q}_{output}$, is the heat transfer rate extracted from the hot tank through the mass flow rate from the hot to the cold salt tank, $\dot{m}_{hot\,to\,cold}$,

$$\dot{m}_{hot\,to\,cold} \cdot C_p \cdot (T_{hot\,tank} - T_{return}) = \dot{Q}_{output}, \quad (2.3)$$

where C_p is the specific heat capacity of salt (assumed constant), and T_{return} is the temperature of the salt flow to the cold salt tank from the power cycle heat exchanger.

Constraints

Table 2.2 provides the constraints considered for the case studies. Four final-point constraints are included to ensure cyclic operation, e.g., the final temperature in the hot tank must equal the initial temperature. The path constraints are due to technological and thermodynamic limitations: the maximum and minimum allowable temperatures of the salt due

Table 2.2: Constraints of optimization

Constraint	Lower Bound	Upper Bound	Description of the Constraint
$T_{hot\,tank}(t_s + 24h)$ [K]	$T_{hot\,tank}(t_s)$	$T_{hot\,tank}(t_s) + 1$	Minimum and maximum allowable final temperature of the hot salt tank
$T_{cold\,tank}(t_s + 24h)$ [K]	$T_{cold\,tank}(t_s)$	$T_{cold\,tank}(t_s) + 1$	Minimum and maximum allowable final temperature of the cold salt tank
$T_{lid}(t_s + 24h)$ [K]	$T_{lid}(t_s)$	$T_{lid}(t_s) + 1$	Minimum and maximum allowable final temperature of the lid
$m_{hot\,tank}(t_s + 24h)$ [kg]	$0.99 \cdot m_{hot\,tank}(t_s)$	$1.01 \cdot m_{hot\,tank}(t_s)$	Minimum and maximum allowable final content of salt in the hot salt tank
T_{salt} [K]	823	873	Minimum and maximum allowable temperature of the salt
T_{lid} [K]	533	–	Minimum allowable temperature of the lid
Q_{output} [MW]	50	100	Minimum and maximum allowable heat transfer rate into the power cycle during operation

to chemical stability and desired steam temperature produced by the steam generator plus the pinch, respectively; the minimum allowable temperature of the lid, being higher than the preheated water temperature at all times so that the second law of thermodynamics is not violated; and the maximum and minimum heat transfer rate into the power cycle, corresponding to full load operation and partial load operation of 50%, respectively. Also, only one plant start-up/shutdown is permitted through the day in order to reduce the thermal stresses suffered by the steam turbine.

2.5 Results

The optimal conditions for the case studies are given in Table 2.3. Figure 2-4 shows the control variable profiles, that is, the profiles of the mass flow rate from the cold tank to the hot tank, and that of the mass flow rate from the hot tank to the cold tank through the power block heat exchanger for the six case studies. In general, $\dot{m}_{cold\,to\,hot}$ follows the heat transfer rate shape collected from the sun to the hot tank, that is, as more heat transfer rate input is available, more salt mass can be heated up. The heat transfer rate collected by the heliostat field into the hot tank, the electric power produced by the power block, and, for the *electrical heating* cases, the electric power purchased from the grid can be seen in Figure 2-5.

2.5.1 Moderately Fluctuating Electricity Price Profile

Under the moderately fluctuating electricity price, the operation strategy where electric heaters are included in the pond gives higher revenue. If the *variable price* case revenue is considered as the base case (100%), *electrical heating* case revenue is 107%, whereas *constant price* case revenue is 57%. As expected, the electric power produced reaches the two limits imposed: maximum power generation when the electricity prices are highest (0.517 $/kWh), and minimum when the electricity prices are lowest (0.224 $/kWh). In *electrical heating* case, the optimizer chooses to purchase electricity from the grid when the price is the lowest. Also, the operation time is higher, 8:30 hours compared to the 6:30 hours of *variable price* case owing to the higher energy transfer into the pond.

2.5.2 Highly Fluctuating Electricity Price Profile

Under the highly fluctuating electricity price, the operation strategy where electric heaters are included in the pond gives higher revenue. If *variable price* case revenue is considered as the base case (100%), *electrical heating* case revenue is 255%. *Constant price* case revenue is extremely low (7%), since the average electricity price is almost zero for the selected day.

Table 2.3: Optimal values for the decision variables $m_{hot\,tank}(t_s)$, $T_{hot\,tank}(t_s)$, $T_{cold\,tank}(t_s)$, $T_{lid}(t_s)$, start-up time, shutdown time, $\dot{m}_{hot\,to\,cold,I}$, and $\dot{m}_{cold\,to\,hot,I}$, and the revenue value

Variable	**Lower Bound**	**Upper Bound**	
$m_{hot\,tank}(t_s)$ [Gg]	0.58	11	
$T_{hot\,tank}(t_s)$ [K]	823	873	
$T_{cold\,tank}(t_s)$ [K]	533	800	
$T_{lid}(t_s)$ [K]	533	873	
Start-up time [h]	N/A	N/A	
Shutdown time [h]	N/A	N/A	
$\dot{m}_{hot\,to\,cold,I}$ [kg/s]	0	250	
$\dot{m}_{cold\,to\,hot,I}$ [kg/s]	0	250	
Variable	**Constant moderately fluctuations**	**Variable moderately fluctuations**	**Electrical Heating moderately fluct.**
$m_{hot\,tank}(t_s)$ [Gg]	7.84	8.98	9.59
$T_{hot\,tank}(t_s)$ [K]	823	823	823
$T_{cold\,tank}(t_s)$ [K]	534	534	534
$T_{lid}(t_s)$ [K]	786	786	785
Start-up time [h]	fixed to 15.1	fixed to 13.4	fixed to 11
Shutdown time [h]	fixed to 21	fixed to 20	fixed to 19.4
$\dot{m}_{hot\,to\,cold,I}$ [kg/s]	Figure 2-4	Figure 2-4	Figure 2-4
$\dot{m}_{cold\,to\,hot,I}$ [kg/s]	Figure 2-4	Figure 2-4	Figure 2-4
Revenue [$]	51,100	91,800	98,400
Variable	**Constant highly fluctuations**	**Variable highly fluctuations**	**Electrical Heating highly fluct.**
$m_{hot\,tank}(t_s)$ [Gg]	4.48	8.87	9.9
$T_{hot\,tank}(t_s)$ [K]	824	823	823
$T_{cold\,tank}(t_s)$ [K]	534	534	534
$T_{lid}(t_s)$ [K]	788	786	785
Start-up time [h]	fixed to 13.4	fixed to 13.7	fixed to 13.8
Shutdown time [h]	fixed to 21.2	fixed to 20.1	fixed to 0.5
$\dot{m}_{hot\,to\,cold,I}$ [kg/s	Figure 2-4	Figure 2-4	Figure 2-4
$\dot{m}_{cold\,to\,hot,I}$ [kg/s]	Figure 2-4	Figure 2-4	Figure 2-4
Revenue [$]	340	5,050	12,900

Maximum electric power output limit is reached during the higher electricity price periods. In the *electrical heating* case, the optimizer chooses to operate the power plant during a negative electricity price period in order to take advantage of the peak electricity price at 6pm which occurs afterwards.

2.6 Discussion

The results clearly demonstrate the significant effect of electric heaters and systematic optimization of time-variable operation on revenue. This can be looked at from two perspectives: 1) the effect of time-variable operation on the revenue. 2) The effect of electricity buy-back from the grid to charge the pond.

In order to assess the economic value added, a comparison of the final revenue in all case studies is considered. The results show that the revenue depends strongly on the operation strategy and electricity price profile. Adding the electric heaters described in Section 2.4, would have an estimated cost of $982,000, allowing for an installation cost of 10% the capital investment. Under highly fluctuating price the revenue difference between *variable price* and *electrical heating* operation strategy is $7,850 per day. An increase in revenue as much as 155% is achieved by adding electric heaters. Under moderately fluctuating price, the difference between both strategies is $6,600. Although the absolute difference is similar to the highly price fluctuations case, the percentage difference is much lower, only 7.2 %, as expected. Consequently, the payback time for both electricity price profiles would be of the order of half a year.

2.7 Conclusions

Herein, optimization case studies were presented for the time-variable operation of the CSPonD solar energy receiver and thermal energy storage, considering time-variable electricity prices and electricity buy-back from the grid. The results show that power production from the CSPonD can be successfully scheduled, assuming the downstream process (i.e.,

the power block) can handle a variable thermal input without drastic losses. Also, revenue maximization is done via scheduling production for time-variant electricity price case studies, while for time-invariant electricity price case studies, the revenue is maximized through minimizing heat losses to the environment. Moreover, herein the competitive advantage of a solar-thermal power plant with thermal energy storage is pointed out, which allows shifting electricity production from low-demand to high-demand times when run in a liberated market. Furthermore, the economic viability of including electric heaters in the thermal energy storage system is shown allowing buying-back electricity from the grid during low-demand times and selling it during high-demand times. Herein, under the moderately fluctuating electricity price profile, the usage of electric heaters increases LCOE because of higher capital cost and lower net electricity output. Under the highly fluctuating electricity price profile, LCOE may also increase (unless the revenue from purchasing electricity at a negative price is accounted for as negative operating cost). Despite the LCOE increase, this strategy is shown to be profitable. Thus, LCOE is misleading not only for different renewable technologies with and without storage, but also for different strategies using the same technology as it does not capture the value of electricity as a function of the TOD. Finally, maximizing revenue via scheduling production is more profitable under highly fluctuating electricity price than under moderately fluctuating electricity price, as expected. Based on these results, a variable FiT is recommended to encourage power production during peak electricity demand hours to avoid power grid overloads. This would give an incentive for energy storage systems, and, thus, for solar-thermal power plants, where inclusion of energy storage systems is more economic than other RES.

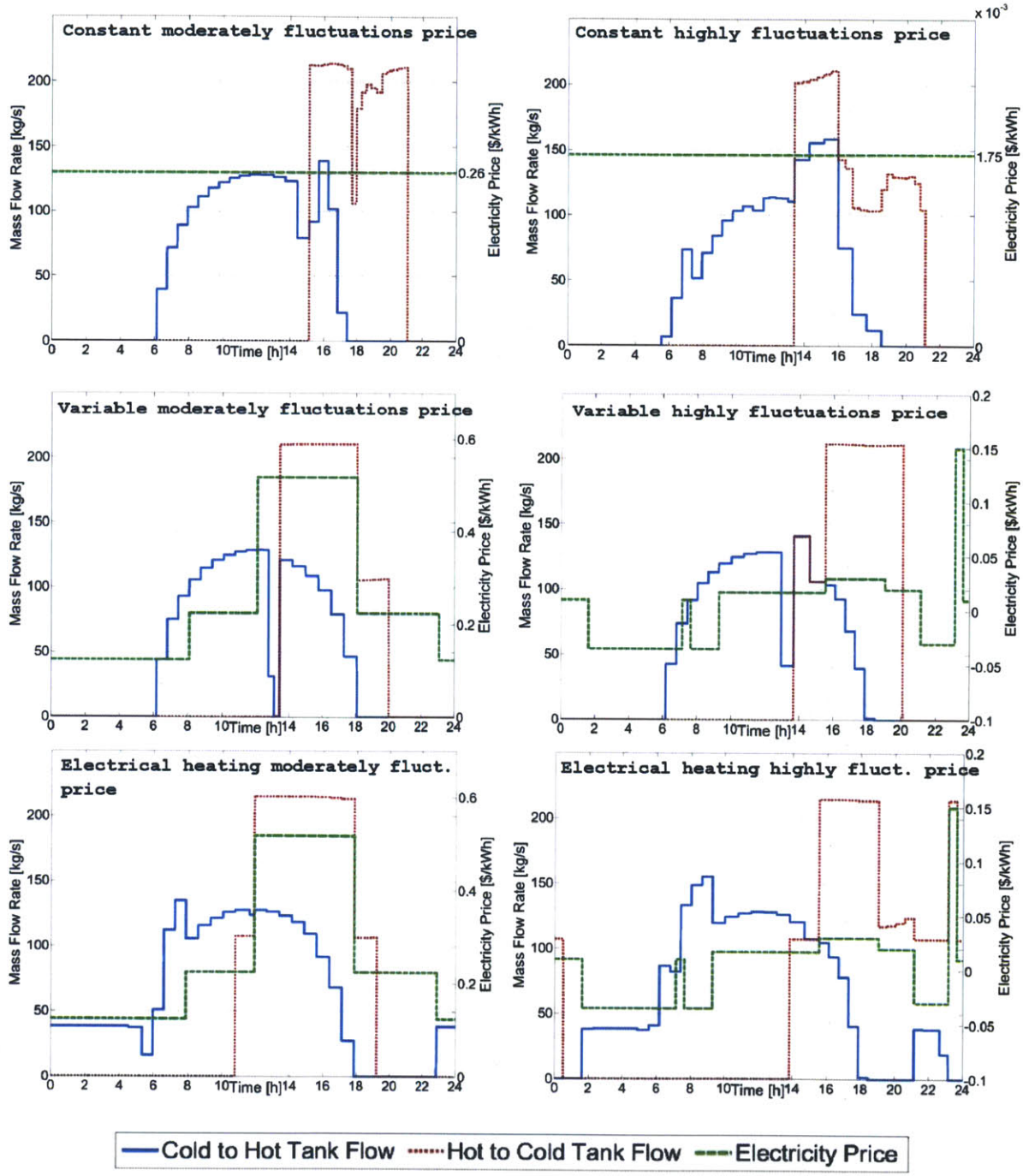

Figure 2-4: Optimal mass flow rate results over the day: solid blue line shows the mass flow rate from the cold to the hot tank, dotted red line shows the mass flow rate from the hot to the cold tank, both referring to the left ordinate [kg/s]; dashed green line shows the electricity price, referring to the right ordinate [$/kWh]

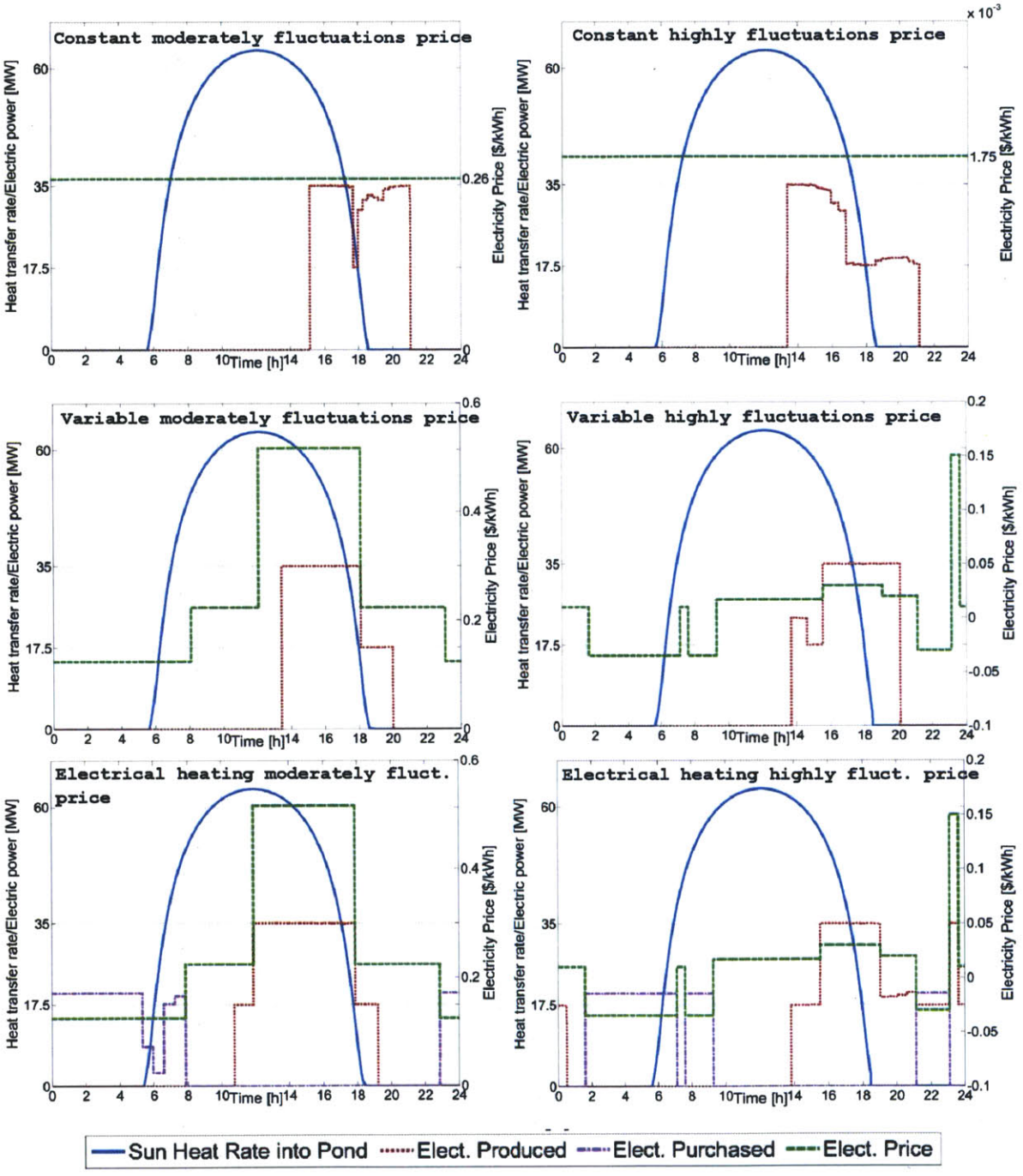

Figure 2-5: Power results over the day: solid blue line shows the heat transfer rate collected by the heliostat field into the hot tank, dash-dotted red line shows the plant electric power output, dotted magenta line shows the electric power purchased from the grid, referring to the left ordinate [MW]; dashed green line shows the electricity price, referring to the right ordinate [$/kWh]

Chapter 3

Performance Analysis of a Regenerative Thermal Storage System with Enhancement Heat Transfer Structures

3.1 Introduction

Several thermal energy storage (TES) concepts have been proposed in solar-thermal energy power plants [18]. This chapter is focused on the design of a regenerative thermal storage system. The regenerator configuration studied is a matrix solid material with an embedded tube heat exchanger (Figure 3-1). The operation in these systems is the following: during charging, thermal energy is transferred from the heat transfer fluid (HTF) to the storage system. At discharging, thermal energy is transferred from the storage system to the HTF, heating up the latter. Herein, an analysis of the discharge process is carried out, with different designs (plain design with no heat transfer structures added, and for different percentages of heat transfer structures added), operation strategies (laminar versus turbulent flow regimes), and dimensions.

Two main types of solid storage concepts without phase change are studied in literature: packed bed, and tube heat exchanger-type thermal energy storage system. A series of articles analyzes the behavior of an oil-pebble bed thermal storage system for a solar cooker computationally [34, 36] and experimentally [35, 37, 33]. In [12], a regenerative thermal storage system with air as the heat transfer fluid and different core geometries and materials for the packed bed is analyzed. [79] analyzes the discharge process of a thermocline thermal energy storage system using molten salt as the heat transfer fluid and rock as filler. Also for the tube heat exchanger type, several studies can be found in literature. In [67] for example, a simulation tool for the analysis of the transient performance of the tube-type storage system with varying material properties and geometries is presented. [27] studies the performance of two new storage materials, high temperature concrete and castable ceramic, with oil as the heat transfer fluid and a tubular heat exchanger integrated into the storage system. [26] presents different strategies to improve storage performance, such as additional structures to enhance heat transfer, and modular storage integration and operation into the solar-thermal power plant concepts. [53] presents a thermal energy storage system with solid as the storage material and gases as the heat transfer fluid. In [29], a similarity analysis of efficiencies of thermal energy storage systems is presented in order to generalize the study of regenerative thermal storage systems. Therein, analysis of a packed bed configuration of solid filler material, and of a thermal storage material with tubes embedded in it where the HTF flows is performed. In the latter case, the storage material considered is liquid, solid, or a mixture of the two.

In the present work, concrete as the solid storage material is studied. Its ease of handling, low cost, and high availability of its raw material all over the world are its main advantages over liquid sensible storage systems. A significant disadvantage is its relatively low thermal conductivity, which makes the charge and discharge processes heat transfer limited. Thus, the time required to use the storage capacity of the system, that is, the complete charge-discharge cycle time, is usually one of the critical features of the system. In solar-thermal power plants, this charge-discharge duration varies from 4 hours to 2 days typically, and

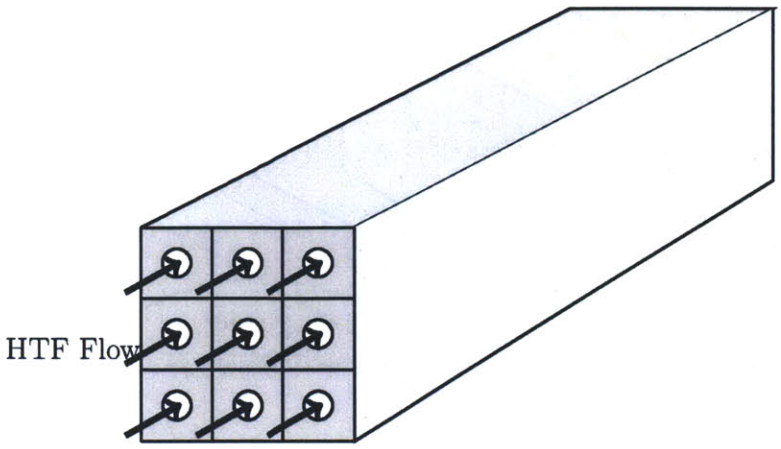

Figure 3-1: Schematic of a solid thermal storage system with an embedded tube heat exchanger

it could go to seasonal time scale. This study focuses on a thermal storage system with a 24-hour operation cycle. To overcome the aforementioned heat transfer limitation, structures to enhance heat transfer have been proposed: fins [27], reinforced bars [8], and plates [58]. These are made of high thermal conductivity materials that speed up the charge and discharge process by decreasing the conductive thermal resistance of the system. The main effect of these heat transfer structures is the decrease of the tube length needed for a fixed thermal energy storage capacity. However, these high thermal conductive materials are more expensive than the matrix material, accounting for a significant share of the system capital cost [67].

Herein, a concrete regenerative thermal storage system is analyzed at the discharge process from a constant uniform initial temperature. The system includes tubes embedded in it where the heat transfer fluid flows through. Different configurations with and without plates as the heat transfer structures, under different flow regimes and storage system dimensions are considered. The specific contribution is a thorough analysis of these different operation strategies and configurations in terms of efficiency, discharge time and specific cost per useful thermal energy capacity.

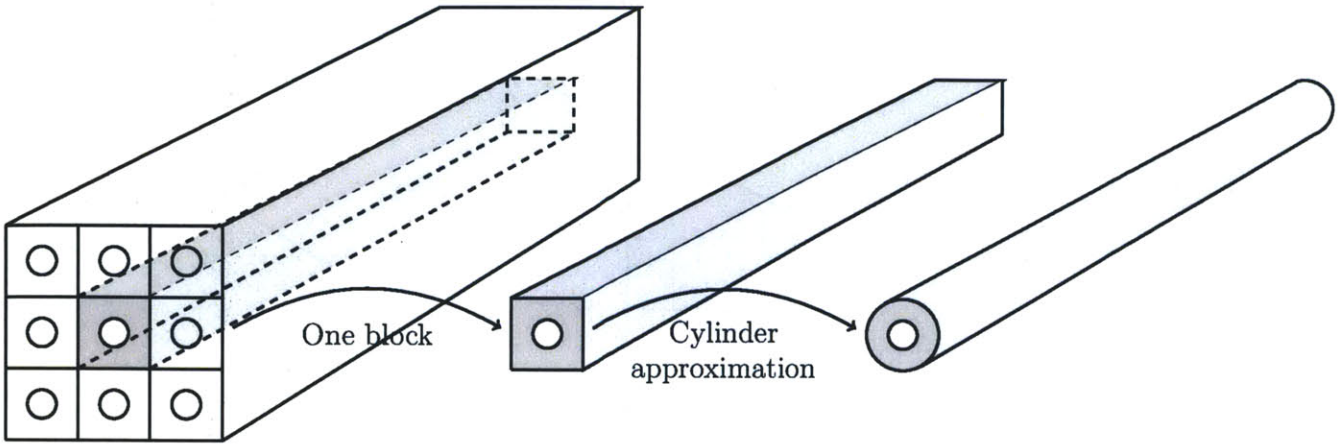

Figure 3-2: Schematic of the solid thermal storage system model as one cylindrical block

3.2 Study Description

The discharge process of a concrete thermal storage system is studied. As depicted in Figure 3-1, the system consists of a voluminous block of concrete, lined with metal tubes through which the heat transfer fluid flows. Initially, the system is at the highest operating temperature T_h, but as the fluid flows through it gradually cools down from T_h to the lowest operating temperature T_c. Because the fluid heats up as it flows through the storage system, the cooling of the concrete is faster at the fluid inlets and slower towards the end, resulting in a temperature gradient throughout the concrete. As it will be explained later in Section 3.3, the materials used are concrete as the matrix material, HITEC solar salt as the HTF, and aluminum for the heat transfer structures. Also, the heat transfer structures are plates. Based on the material properties, the highest operating temperature is $T_h = 600°C$, and the lowest is $T_c = 250°C$. These temperatures are based on the limits of solar salt: chemical stability in the upper temperature, and freezing temperature (~ 220°C) in the lower one [5]. In the present study, the storage system is analyzed by a cylindrical approximation of one of its blocks (Figure 3-2). As will be explained in Section 3.4, a 2-dimensional model with material properties independent of temperature is used.

3.2.1 Parameters description

Before addressing the material selection and model description and assumptions, the current section provides the equations of several important quantities used in the remainder of the thesis.

The dimensional parameters that characterize each storage configuration are the tube diameter, d, the external diameter, D, and the length of the storage device, L (Figure 3-3). The heat transfer structures are added in the form of plates with thickness δ_{plate}. The relative amount of heat transfer structures added b, is calculated based on the volume percentage with respect to the total solid volume, that is,

$$b = \frac{\text{Heat transfer structures volume}}{\text{Total solid material volume}} = \frac{\frac{\pi}{4}(D^2 - d^2)\,\delta_{plate} N}{\frac{\pi}{4}(D^2 - d^2)\,L} = \frac{\delta_{plate} N}{L}, \tag{3.1}$$

where δ_{plate} is the plate thickness, and N is the number of plates used. The total thermal energy capacity of each block is calculated as

$$\begin{aligned} U_{th} &= \Big((\rho c_p)_{HTF} \frac{\pi}{4} d^2 L + (\rho c_p)_{metal} \frac{\pi}{4} (D^2 - d^2) \delta_{plate} N \\ &\quad + (\rho c_p)_{concrete} \frac{\pi}{4} (D^2 - d^2)(L - \delta_{plate} N) \Big) (T_h - T_c), \end{aligned} \tag{3.2}$$

where ρ_i is the density of material i, and and $c_{p,i}$ is its specific heat capacity, for i = HTF (solar salt herein), metal (aluminum herein), and concrete. It is worth noting that the operation temperatures difference is included in the calculation of U_{th} to obtain the actual capacity of the storage system. The design system heat transfer output of each block is calculated as

$$\dot{Q} = \dot{m}_{HTF} c_{p,HTF} (T_h - T_c), \tag{3.3}$$

where $\dot{m}_{HTF}$ is the design HTF mass flow rate, calculated as

$$\dot{m}_{HTF} = \frac{\pi}{4} d^2 \rho_{HTF} u_{in}, \tag{3.4}$$

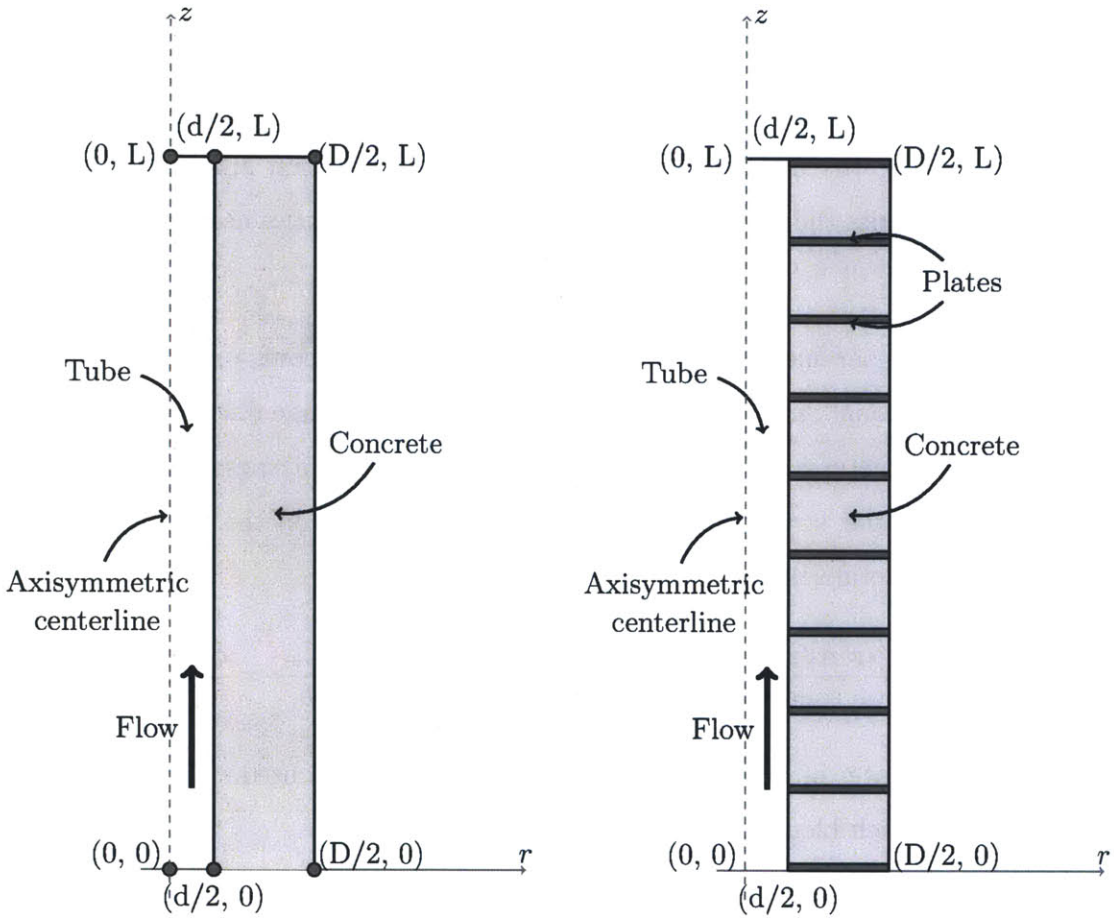

Figure 3-3: 2-D axisymmetric model: without heat transfer structures (left) and with heat transfer structures added as equidistant plates (right)

where u_{in} is the design average inlet velocity. The system heat transfer output at time t is calculated as

$$\dot{Q}(t) = \dot{m}_{HTF}(t) c_{p,HTF}(T_{bulk}(L,t) - T_c), \tag{3.5}$$

where $\dot{m}_{HTF}(t)$ is the HTF mass flow rate at time t, and $T_{bulk}(L,t)$ is the fluid bulk temperature at length L and time t. $\dot{m}_{HTF}(t)$ is calculated as

$$\dot{m}_{HTF}(t) = \frac{\pi}{4} d^2 \rho_{HTF} \bar{u}_z(t), \tag{3.6}$$

where $\bar{u}_z(t)$ is the average velocity in the z direction at time t

$$\bar{u}_z(t) = \frac{\int 2\pi r u_z(r,z,t)dr}{\int 2\pi r dr}. \tag{3.7}$$

$\bar{u}_z(t)$ is independent of z by mass continuity because the HTF is incompressible. The fluid bulk temperature $T_{bulk}(z,t)$ at length z and time t is calculated as

$$T_{bulk}(z,t) = \frac{\int 2\pi r u_z(r,z,t)T(r,z,t)dr}{\int 2\pi r u_z(r,z,t)dr}. \tag{3.8}$$

The non-dimensional bulk temperature $\theta_{bulk}(z,t)$ at length z and time t is calculated as

$$\theta_{bulk}(z,t) = \frac{T_{bulk}(z,t) - T_c}{T_h - T_c}, \tag{3.9}$$

and thus $\theta_{bulk}(z,t) \in [0,1]$. The total thermal energy output for the entire discharge period is calculated as

$$Q_{output} = \int_0^{\tau_{discharge}} \dot{m}_{HTF}(t) c_{p,HTF}(T_{bulk}(L,t) - T_c)dt, \tag{3.10}$$

where $\tau_{discharge}$ is the discharge time period, calculated as the time period where the non-dimensional bulk outlet temperature $\theta_{bulk}(L,t)$ (monotonically decreasing in time) is equal to a certain coefficient θ_0,

$$\theta_{bulk}(L, \tau_{discharge}) = \theta_0. \tag{3.11}$$

This calculation reflects the need of $T_{bulk}(L,t)$ to be at a high temperature so that it is useful for the consequent power block. In the present study, $\theta_0 = 0.9$, that is, HTF delivers useful energy while its bulk temperature is higher than 565°C, an appropriate value for Rankine cycles, the thermodynamic cycles typically used in solar-thermal power plants. The discharge efficiency is calculated as the ratio of the total thermal energy output during the discharge period to the total thermal energy capacity

$$\eta_{discharge} = \frac{Q_{output}}{U_{th}}. \tag{3.12}$$

The discharge efficiency quantifies the system capacity to deliver useful thermal energy to the power block. A high discharge efficiency is also desirable for the discharge-charge cycle. Firstly, the storage system temperature has to be close to T_c after the discharge process so that the system capacity available to store thermal energy is close to its design one U_{th} for the charge process. Secondly, the temperature difference (which is the driving force of heat transfer processes) between the cold storage material and the hot solar salt is higher favoring the heat transfer process. The same applies for the charge efficiency. It is worth noting that the values sought for the discharge time and efficiency are interdependent for the decision of the storage configuration design: high efficiency is sought together with low discharge time. For example, a storage system where the heat losses are of similar order of magnitude of Q_{output} would have a lower discharge time than the same system with no heat losses. However, the discharge efficiency will be at most 0.5, a bad design value, and lower than for the second system, making it a bad storage configuration design.

The ratio of the tube cross sectional area to the total cross sectional area is calculated by

$$\epsilon = \frac{A_{tube}}{A_{total}} = \frac{\frac{\pi}{4}d^2}{\frac{\pi}{4}D^2} = \frac{d^2}{D^2}. \tag{3.13}$$

This is an important metric used to present the results. It reflects the ratio of HTF volume to total volume of the regenerator. Also, ϵ is an indirect measurement of the amount of piping used. For equal tube diameter d, low ϵ implies high block diameter D, which implies high distance between tubes. As a consequence, for two storage configurations with equal U_{th} and $\eta_{discharge}$ operating with the same $\dot{m}_{HTF}$ (that is, for two storage configurations with the same performance specifications $\dot{Q}$ and Q_{output}), less tube length L is needed (Figure 3-4). Tube length accounts for some important capital costs, such as piping material, and HTF, and operating costs, such as pumping power. The main effect of the heat transfer structures is the decrease of the conductive thermal resistance allowing for designs with higher D (lower ϵ). In order to analyze the economic advantage of the high conductive added material, different configurations are compared. High discharge efficiency can be sought through the addition of heat transfer structures, and also by the increase of storage length. For a fixed tube

diameter and mass flow rate, the counterpart of the latter is that the discharge time is also higher because both there is more heat transfer area and the time to reach the storage outlet is higher, limiting the viability of using it in a solar-thermal power plant. These trade-offs are studied in the presented study, and shown later in Section 3.7, where the cost per kWh_{th} versus discharge time and versus efficiency is plotted.

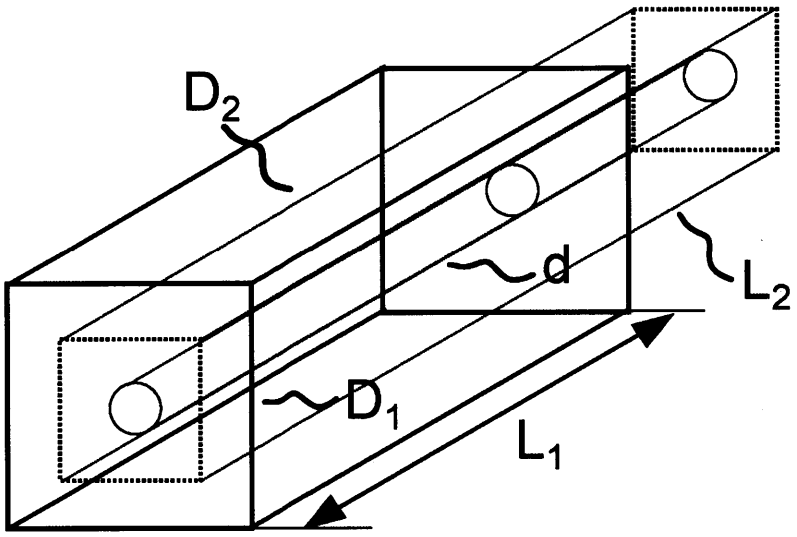

Figure 3-4: Two blocks of equal total thermal capacity U_{th} and tube diameter d: one obtained with short L_1 and large D_1, the other with larger L_2 and shorter D_2 (not on scale)

3.2.2 Motivation

The objective of adding the high thermal conductive material is to decrease the thermal resistance of the storage material in the radial direction. This favors the heat transfer from the HTF to the solid material during the charge process, and vice versa during the discharge process. At the same time, heat transfer within the solid material in the longitudinal direction affects negatively the performance of the regenerator since it decreases the storage maximum temperature at the outlet and increases the storage lowest temperature at the inlet, decreasing its exergy. Thus, the heat transfer structures should not decrease the longitudinal thermal resistance significantly. Moreover, the convective thermal resistance of

the fluid flow has to be also taken into account. One way to decrease it is operating in the turbulent regime, where the heat transfer coefficient is increased significantly compared to the laminar regime. The parameter that determines the laminar or turbulent regime is the Reynolds number based on the tube diameter

$$Re_d = \frac{\rho_{HTF} u_{in} d}{\mu_{HTF}}, \tag{3.14}$$

where μ_{HTF} is the dynamic viscosity of the HTF. For $Re_d < 2,300$, the flow is in the laminar regime. For $Re_d > 10,000$, the flow is in the turbulent regime. Between 2,300 and 10,000 is the transition regime, where the operation is not recommended since the heat transfer can not be calculated. For a fixed tube diameter d, the counterpart of operating at the turbulent regime is that the mass flow rate is higher than in the laminar regime, so the required heat transfer rate to increase the fluid temperature is also higher.

For cylindrical coordinates, the radial conductive thermal resistance between two radii r and r_0 for a length l is

$$R_r = \frac{\log(r/r_0)}{2\pi k l}, \tag{3.15}$$

and the longitudinal thermal resistance for a cross sectional A_{cross} and a length l is

$$R_z = \frac{l}{k A_{cross}}. \tag{3.16}$$

For a cylindrical tube with a inner diameter d_{in} and outer diameter d_{out}, $A_{cross} = \frac{\pi}{4}(d_{out}^2 - d_{in}^2)$. The convective thermal resistance for a convective heat transfer coefficient h and a surface area $A_{surface}$ is

$$R_h = \frac{1}{h A_{surface}}. \tag{3.17}$$

For a cylinder of diameter d_{in} and length l, $A_{surface} = \pi d_{in} l$.

The best arrangement to obtain this is to add the high conductivity material in the form of thin plates, instead of reinforced bars, as it is shown later. After a detailed description of the model and an analysis of the different model possibilities and assumptions, several

configurations of the thin plate model will be investigated with respect to the discharge efficiency, discharge time, and storage cost.

3.3 Selection of Structure Materials

As stated above, the thermal storage system studied herein is based on materials which do not experience phase change over the temperature range of operation. In literature, this group of materials are called sensible heat storage materials. The desirable characteristic of any TES material are longevity, inexpensiveness, high volumetric capacity ρc_p, high thermal diffusivity $\alpha = \frac{k}{\rho c_p}$, easy start-up, chemical stability at the operating temperature range, similar coefficient of thermal expansion (CTE) to other materials that are part of the system such as heat transfer structures or piping. High volumetric capacity reduces storage volume for the same thermal energy capacity and operation temperature range. High thermal diffusivity increases the dynamics of the process speeding up the transients by increasing the heat transfer rate. For some sensible liquid TES such as solar salt, the start-up is troublesome due to its high freezing temperature (220°C, Table 3.3) and low thermal conductivity in the solid phase (~ 0.5 W/(m·K)), which make the melting process from ambient temperature complicated. A similar CTE among the materials that form the system reduces thermal stresses that can reduce its operational life.

Table 3.1 shows the principal characteristics of the most common solid thermal storage materials. Laing et al. [27] recently developed two new storage materials, a castable ceramic based on a binder containing Al_2O_3, and a high temperature concrete to improve the soft characteristics of concrete. According to [27], high temperature concrete seems to be more favorable to use over castable ceramic due to the lower cost and easier handling of the premixed material. The high temperature concrete mixture is similar to regular concrete used in construction: mainly blast furnace cement as a binder system, aggregates (temperature resistant gravel and sand), and a small amount of polyethylene fibers [25]. Thus, in the present study its the cost is approximated by 0.05 \$/kg, the same as reinforced concrete. As explained later on, high temperature concrete is chosen as the TES material in the study.

The main disadvantage of this material for application as the thermal storage medium is its low thermal conductivity (1.3 W/(m·K)), which limits the heat transfer rate, slowing down the dynamics of the system.

To overcome this issue, high conductivity materials are considered to be added to the system to enhance heat transfer. Table 3.2 shows possible materials. The desirable characteristics of the high conductivity material are high thermal conductivity and low cost per volume (so that more heat transfer structure volume can be included at a same price). Among the materials of Table 3.2, aluminum is the cheapest in $ per volume. Also, it has the same order of magnitude thermal conductivity as copper, which accounts for the highest thermal conductivity among the materials considered, whereas aluminum is 10 times cheaper than the latter. Thus, aluminum is the best option.

Regarding the heat transfer fluid choice, several aspects are to be taken into account. In this application, the volume of the regenerator tubes is not negligible, thus, it is desirable that the fluid has not only good heat transfer properties and low cost, but also good thermal energy storage properties. Table 3.3 shows the principal characteristics and costs of different sensible heat storage liquid materials [23], with similar values reported in [18, 48].

The selection of the TES and HTF material is interdependent since their operating temperatures should match. High maximum storage temperature is desirable in order to have high exergy storage system. Also, a wide operation temperature range saves TES material for the same thermal energy capacity for constant volumetric heat capacity ρc_p. At the same time, material cost is also important. Looking at Table 3.3, HITEC solar salt can reach higher temperatures than oil and other salts, and its cost is also lower. Its principal disadvantage is the high melting temperature. The average solar salt properties used are taken from [5]. Looking at Table 3.1, the materials that withstand up to 600°C are cast steel, silica fire bricks, and magnesia fire bricks. Also, high temperature concrete has be successfully tested up to 500°C recently [25]. Herein, it is assumed that high temperature concrete can operate up to a temperature of 600°C (current research is projected in this direction [57]). These materials have similar storage capacity. However, the high temperature concrete cost

per kg is about two orders of magnitude less than that of the other materials. Thus, the combination of high temperature concrete as the TES material and HITEC solar salt as the HTF is selected in this study.

The corrosion rate of the piping material needs to be low over the operation temperature range. Although the nitrate salt is relatively benign in terms of corrosion potential, the industrial grade of the salt does contain impurities, of which the most chemically active are the chlorides and perchlorates [23]. According to [6], cast steels are the materials that better resist corrosion. The same is also reported in [24, 23]. In the current design, cast steel has therefore been selected as the piping material.

3.4 Mathematical Model

The physical problem of the thermal energy storage system discharge is transient conjugate heat transfer. The conjugate nature is inherent to any passive TES, since the intention of heat transfer is an interaction between at least two mediums. Also, it is transient due to the nature of the thermal storage system: storage charge and discharge imply non-steady state periods of time.

3.4.1 Literature Review and Historical Perspective

Herein, a brief literature review of the transient forced convection analytical and numerical studies in ducts is presented. In early works, approximate analytical methods were used. The main methods are self-similar solutions of the boundary layer equations, solutions of the boundary layer equations in the power series, integral methods, the method of superposition, and solutions of the boundary layer equations in the series of shape parameters [9]. Sucec used similar methods to solve the unsteady conjugated forced convection heat transfer problem in a parallel plate duct with inlet fluid temperature varying periodically in time [66], in the thermal entrance region of a duct where the unsteadiness is caused by a sudden change in ambient temperature [63], and in a parallel plate duct where there is

Table 3.1: Characteristic of thermal energy storage solid materials

Material	**Sand-rock-mineral oil** [14]	**Reinforced concrete** [14]	**NaCl (solid)** [14]	**Cast iron** [14]	**Cast steel** [14]	**Silica fire bricks** [14]	**Magnesia fire bricks** [14]	**High temperature concrete @370°C** [26, 27, 25]	**Castable ceramic @350°C** [26, 27]
Lower T [°C]	200	200	200	200	200	200	200	250	250
Higher T [°C]	300	400	500	400	700	700	1,200	500	400
Average ρ [kg/m^3]	1,700	2,200	2,160	7,200	7,800	1,820	3,000	2,250	3,500
Average k [W/(m·K)]	1.0	1.5	7.0	37.0	40.0	1.5	5.0	1.3	1.35
Average c_p [J/(kg·K)]	1,300	850	850	560	600	1,000	1,150	1,100	866
Capacity [kWh$_t$/(m^3·K)]	0.6	0.5	0.5	1.12	1.3	.55	0.95	0.68	0.84
Volume specific heat capacity [kWh$_t$/m^3]	60	100	150	160	450	150	600	170	126
Cost per kg [$/kg]	0.15	0.05	0.15	1.00	5.00	1.00	2.00	0.05	n.a.
Storage cost [$/kWh$_t$]	4.2	1.0	1.5	32.0	60.0	7.0	6.0	0.66	n.a.

Table 3.2: High thermal conductivity materials [39, 42]

Material	**Steel**	**Aluminum**	**Iron**	**Copper**
ρ [kg/m^3]	7,850	2,700	7,900	8,960
c_p [J/(kg·K)]	475	900	452	422
Capacity [kWh$_t$/(m^3·K)]	1.04	0.675	1.65	1.05
α [m^2/s]	$1.19 \cdot 10^{-5}$	$8.27 \cdot 10^{-5}$	$2.25 \cdot 10^{-5}$	$9.92 \cdot 10^{-5}$
k [W/(m·K)]	44.5	201	80.4	375
CTE [μm/(m·K)]	12.3	23.4	11.8	17
Cost per kg [$/kg]	5	2.3	1	8.7
Cost per m^3 [$/m^3]	39,250	6,291	7,900	77,952

sinusoidal wall heat generation along the axial position [65]. In his work, Sucec used the so-called improved quasi-steady approach [62], taking into account the thermal history and thermal energy storage capacity of the flowing fluid. As an example of a solution in asymptotic series in eigenfunctions, [45] analyzes the transient conjugated heat transfer problem in the hydrodynamically and thermally fully developed region of a laminar pipe flow under a constant wall temperature and constant wall heat flux. Also, several researchers use the plug flow approximation to study transient coupled heat transfer when unsteadiness is caused by flow with time-varying inlet temperature, by step inlet temperature change, or by unsteady boundary conditions in the wall: [61] analyzes the unsteady laminar heat transfer in a duct with periodically varying inlet temperature and time- and space-dependent wall temperature, using the quasi-steady assumption which leads to an eigenvalue problem in which the eigenvalues are complex. In [59], laminar heat transfer in a channel with unsteady flow and wall heat flux varying with position and time. [50] shows the analysis of a laminar flow in a duct with unsteady heat addition where the transient processes are caused by changing the fluid pumping pressure and either the wall temperature or the wall heat flux. In [21], response to a step increase in wall temperature is analyzed. In the latter three articles, thermal conditions at the wall are specified and the fluid inlet temperature is constant. [68]

Table 3.3: Characteristic of heat transfer fluids [23]

Material	**Solar Salt**	**Hitec**	**Hitex XL (Calcium Nitrate Salt)**	**$LiNO_3$**	**Therminol VP-1**
Composition, %					biphenyl/ diphenyl oxide
$NaNO_3$	60	7	7		
KNO_3	40	53	45		
$NaNO_2$		40			
$Ca(NO_3)_2$			48		
Freezing T [°C]	220	145	120	120	13
Max. T [°C]	600	535	500	550	400
ρ@300°C [kg/m^3]	1,899	1,640	1,992	n.a.	815
μ@300°C [cp]	3.26	3.16	6.37	n.a.	0.2
c_p@300°C [J/(m^3·K)]	1,495	1,560	1,447	n.a.	2,319
Cost per kg [$/kg]	0.49	0.93	1.19	1.19	2.2
Storage cost [$/kWh$_t$]	5.8	10.7	15.2	15.0	28.75

analyzes the transient laminar forced convection in the thermal entrance region of a circular duct with a periodically varying inlet temperature and convection from the ambient medium with a constant heat transfer coefficient. Duct wall heat capacity is taken into account. The problem is solved applying the Laplace transform so that complex eigenvalues are avoided.

With randomly varying boundary conditions, or when more features are included in the study, such as the thermal capacity of the fluid and the wall, numerical methods are used. [28] analyzes the transient conjugated forced convection heat transfer with fully developed laminar flow in a pipe with a constant wall temperature at the external surface for a certain length. Lee and Yan [28] use a finite-difference scheme to solve the problem. The same problem under different boundary conditions is found in the following four articles: in [30], uniform wall heat flux is applied, whereas in [78] constant wall temperature is considered. The case of an ambient temperature step change is analyzed for laminar [76], and turbulent flow regime [77]. In [64], the unsteadiness comes from the sudden exposure of the outside of the duct walls to an ambient fluid with a constant heat transfer coefficient. In [1, 56] the effects of both the heat transfer and laminar flow transients are analyzed using a finite-different scheme for the former case, and a control volume approach for the latter study. In [7], a second-order finite-difference scheme is used to solve a inlet temperature step change for a parallel-plate duct.

In research related to solid thermal storage systems, a finite difference scheme method is used in a series of articles [27, 67, 26]. In [26], a finite element method analysis is also used for a segment of a storage pipe embedded in concrete with and without axial fins. In [53], the authors develop a two-dimensional simulation model to numerically determine the dynamic temperature and velocity profiles of gases and solid heat-storing materials in a composite material honeycomb regenerator.

3.4.2 Mathematical Model: Description and Assumptions Validation

Herein, the thermal energy storage system is reduced to the approximation of one block as a cylinder, shown in Figure 3-2. An axisymmetric 2-dimensional transient finite element model (FEM) is used. COMSOL Multiphysics® [39] is used as the modeling software. MATLAB® [32] is used for the results post-process. As explained above, properties are independent of temperature. Thus, the fluid flow and the heat transfer problems are uncoupled. Also, as will be shown in Section 3.4.2, plug flow is a good approximation for this study reducing the conjugated problem to a heat transfer one. The problem is not thermally fully developed. To characterize the discharge time and efficiency, the system is assumed to be completely charged. That is, its temperature is uniform and corresponds to the highest, $T_{system}(t = 0) = T_h$. HITEC solar salt enters the block at the lowest temperature allowable, $T_{inlet} = T_c = 250°C$. The inlet velocity u_in is calculated by Re_d and d of each case study. Herein, Re_d = 500, 1,000, and 10,000 are considered, as will be shown later. Also, the system is considered thermally insulated. Figure 3-5 shows the initial and boundary conditions. In order to avoid numerical artifacts due to conflict between the initial and the boundary condition temperatures, the inlet temperature is approximated using the built-in smooth step function in COMSOL. The extent of this step function, 50 s, has negligible effect on the discharge process.

Viscous dissipation is not considered. The equation to be solved is the energy balance for both the fluid and the solid. In cylindrical coordinates, the energy equation for axisymmetric plug flow is reduced to

$$\rho c_p \left(\frac{\partial T}{\partial t} + u_z \frac{\partial T}{\partial z} \right) = \frac{k}{r} \frac{\partial}{\partial r} \left(r \frac{\partial T}{\partial r} \right) + k \frac{\partial^2 T}{\partial z^2}, \tag{3.18}$$

and for the solid material

$$\rho c_p \frac{\partial T}{\partial t} = \frac{k}{r} \frac{\partial}{\partial r} \left(r \frac{\partial T}{\partial r} \right) + k \frac{\partial^2 T}{\partial z^2}. \tag{3.19}$$

The model assumptions and values of physical properties used are:

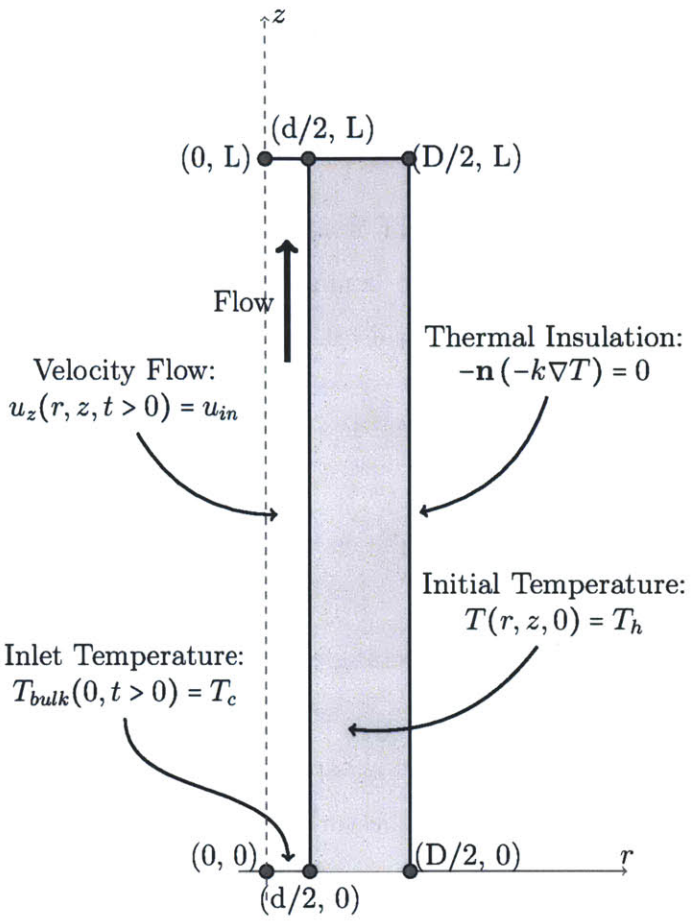

Figure 3-5: 2-D axisymmetric model initial and boundary conditions: initially at the maximum temperature ($T(r, z, 0) = T_h$), and thermally insulated at every boundary ($-\mathbf{n}(-k\nabla T) = 0$) besides at the inlet, where the inlet temperature is the minimum ($T_{bulk}(0, t) = T_c$).

- A structured mesh is used.
- The piping material is not included in the model, although it is accounted in the storage cost calculation.
- The pipe flow is modeled as a plug flow.
- The discharge process is analogous to the charge process.
- Equivalent material properties model with the cases with heat transfer structures

added.

- Three configurations for the heat transfer structures are tested for a case configuration, for the final parametric studies only plates are studied as they perform best.

- The thermal conductivity of the HTF fluid has been adjusted from the material value 0.54 to 0.36 W/(m·K) for d = 0.1 m laminar flow, and to 30 W/(m·K) for d = 0.05 m turbulent flow, and 15 W/(m·K) for d = 0.1 m turbulent flow.

The derivation of the given values as well as a detailed validation of the listed assumptions is given in the following sections.

Structured Mesh

A structured or mapped mesh with rectangles elements is used due to its ease parameter specification. The maximum element size is set to 0.03 m for laminar flow cases, and 0.3 m for turbulent flow cases. The difference is explained because the length needed to obtain good discharge efficiencies is higher for the turbulent cases than that ones in the laminar regime. The minimum element size is set to 0.01 m. Also, the fluid cross sectional length is divided in 4 elements, given that the resultant elements' size is between the previous specified values 0.01-0.03/0.3 m. In the case of the solid domain, the cross sectional length is divided into 6 elements, given that the resultant elements' size is between the previous specified values 0.01-0.03/0.3 m. In the longitudinal direction, the element size is equal to the maximum value, 0.03/0.3 m, besides in the aluminum plates domains, where the longitudinal element size is equal to 0.01 m to match the plate thickness δ_{plate}. Table 3.4 shows the mesh general parameters. Theses values are obtained in the following manner: starting from a coarse mesh, refine it until no changes are observed. In the radial direction, no change is obtained with the mesh with 4 elements in the fluid domain and 6 in the solid domain from a mesh divided by 3 and 5 elements, respectively, for ϵ = 0.1. In the longitudinal direction, for turbulent flow, same discharge time and a discharge efficiency that differs in 0.01% is calculated for two meshes with maximum length 0.3 m and 0.01 m, respectively, for a storage

Table 3.4: Mesh features

Size parameter	**Plug flow Re_d < 2,300 and laminar flow**	**Plug flow Re_d > 10,000**
Max. element size [m]	0.03	0.3
Min. element size [m]	0.01	0.01
Element shape	Rectangle	Rectangle

length of 500 m, the lowest among the ones studies in the turbulent regime. A coarser mesh could have been used. Similar results for the mesh parameters in the laminar cases.

Convective heat transfer coefficient calculation

The Nusselt number based on the tube diameter is defined as

$$Nu_d = \frac{hd}{k_{HTF}}, \tag{3.20}$$

where h is the convective heat transfer coefficient, and k_{HTF} is the HTF thermal conductivity. The results of the FEM code have been validated under constant boundary conditions for which Nu_d is constant, by comparing the Nu_d calculated based on the simulations results with analytical values found in literature. The convective heat transfer coefficient between the fluid flow and the solid storage at a length z and time t is calculated by

$$h(z,t) = \frac{\dot{q}(z,t)}{T_{bulk}(z,t) - T_{wall}(z,t)}, \tag{3.21}$$

where $\dot{q}(z,t)$ is the wall heat flux at length z and time t [W/m^2], $T_{bulk}(z,t)$ is the fluid bulk temperature at length z and time t, and $T_{wall}(z,t)$ is the wall temperature at length z and time t. In order to calculate the three terms of equation (3.21), a rigid control volume (CV) study is performed (Figure 3-6). The CV is placed inside the tube with a length l small in comparison with the total tube length L ($\frac{l}{L} \sim 10^{-3}$). $T_{bulk}(z,t)$ is approximated

by the arithmetic average $\bar{T}_{bulk}(z,t)$ at the inlet and outlet of the CV. On the other hand, $T_{wall}(z,t)$ is taken as the average wall temperature along the CV length l, $\bar{T}_{wall}(z,t)$. To calculate $\dot{q}(z,t)$, the first law of thermodynamics is applied:

$$\frac{dE(t)}{dt} = \dot{Q}(t) - \dot{W}(t) + (\dot{m}_{HTF}(t)h(t))_{in} - (\dot{m}_{HTF}(t)h(t))_{out}, \tag{3.22}$$

where $E(t)$ is the internal energy of the material inside the CV at time t [J], $\dot{Q}(t)$ is the heat transfer rate into the CV at time t [W], $\dot{W}(t)$ is the work rate done by the CV at time t [W], and $(\dot{m}_{HTF}(t)h(t))_{in}$ and $(\dot{m}_{HTF}(t)h(t))_{out}$ is the energy rate into and out of the CV carried by the fluid flow at time t [W]. Herein, $\dot{W}(t)$ is zero. Also,

$$(\dot{m}_{HTF}(t)h(t))_z = \dot{m}_{HTF}(z,t)c_{p,\,salt}T_{bulk}(z,t) = \int 2\pi r \rho_{salt} u_z(r,z,t) c_{p,\,salt} T(r,z,t) dr. \tag{3.23}$$

$\frac{dE(t)}{dt}$ is approximated by

$$\frac{dE(t)}{dt} \approx \frac{E(t) - E(t')}{\Delta t}, \tag{3.24}$$

where $t' = t - \Delta t$, $\Delta t = 100s$, and

$$E(t) = \int \int_{CV} 2\pi r \rho_{salt} c_{p,\,salt} T(r,z,t) dr dz. \tag{3.25}$$

From equation (3.22), and by calculating integrals (3.23) and (3.23), $\dot{Q}(z,t)$ is obtained, and $\dot{q}(z,t)$ follows from

$$\dot{q}(z,t) = \frac{\dot{Q}(z,t)}{\pi l d}. \tag{3.26}$$

Thus, with $\dot{q}(z,t)$, and calculating $T_{bulk}(in,t)$, $T_{bulk}(out,t)$ and $\bar{T}_{wall}(z,t)$ from simulation results, the only remaining unknown in equation (3.21) is $h(z,t)$.

Following this procedure Nu_d of laminar and plug flow stationary problems with constant wall temperature and constant heat flux at the hydrodynamically and thermally fully developed regions is calculated. Therein, Nu_d is constant and known (values shown in Table 3.5). The calculated values match completely the analytical ones. Thus, the method is validated, with the exception of the time differential term.

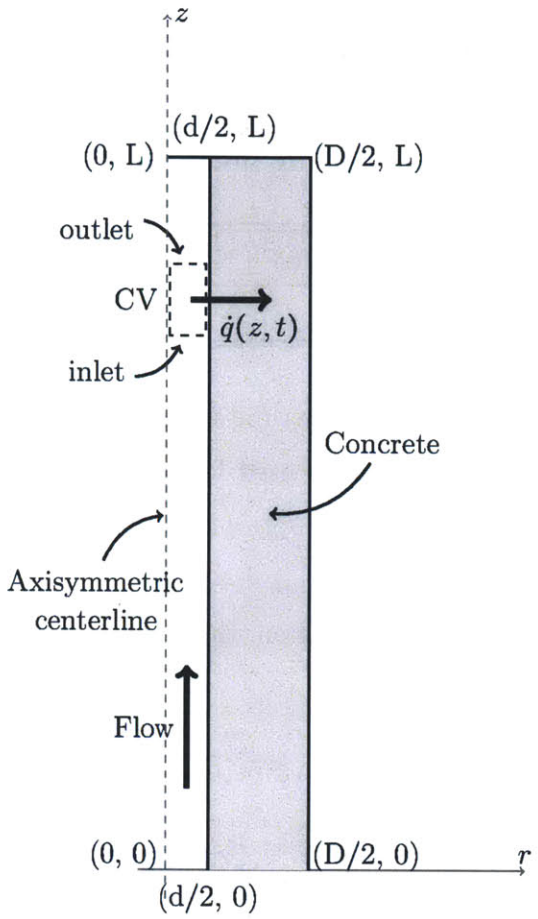

Figure 3-6: Schematic of the rigid Control Volume (CV) used to calculate the convective heat transfer coefficient, h

Tube pipe

As discussed in Section 3.3, cast steel is used as the piping material. Although it is accounted in the storage cost calculation, its effect on heat transfer and storage capacity is not modeled. Its thermal resistance is negligible in the radial direction, and high in the longitudinal direction. In the radial direction, the pipe thermal resistance is in series with the concrete thermal resistance,

$$\text{Radial resistance: } R_{r,eq} = R_{r,steel} + R_{r,concrete}. \tag{3.27}$$

Table 3.5: Nu_d for laminar and plug flow under constant boundary conditions at hydrodynamically and thermally fully developed flow: analytical and calculated values

	Analytical value		**Calculated value**	
Case	**Laminar** ($Re_d <$ 2,300) **[38]**	**Plug flow [40]**	**Laminar** $Re_d = 1,000$	**Plug flow** $Re_d = 1,000$
Const. T_{wall}	3.66	5.783	3.7	5.8
Const. $\dot{q}$	4.364	8	4.4	8

The pipe wall thickness δ_{pipe}, depends on the tube diameter. In literature, for a tube diameter of 2.06 cm, a wall thickness of 1.2 mm is used for nitrate salt [71]. Assuming a relation between the diameter and thickness, herein δ_{pipe} = 2 mm is assumed, since the tube diameters considered are larger: d = 0.05, 0.1 m. k_{steel} = 40 W/(m·K), and the lowest value of D/d considered is 1.4. Thus, in the radial direction, the respective thermal resistances orders of magnitude, calculated from (3.15), are:

- Cast steel radial resistance by unit length: $R_{r,\,steel} = \frac{\log(d/(d-2t))}{2\pi k_{steel}} \sim 10^{-4}$ [(K·m)/W]
- Concrete radial resistance by unit length: $R_{r,\,concrete} = \frac{\log(D/d)}{2\pi k_{concrete}} \sim 10^{-2}$–$10^{-1}$ [(K·m)/W]

Thus, $R_{r,steel} << R_{r,concrete}$, validating the approximation. In the longitudinal direction, pipe and concrete thermal resistances are in parallel

$$\text{Longitudinal resistance: } \frac{1}{R_{z,\,eq}} = \frac{1}{R_{z,\,steel}} + \frac{1}{R_{z,\,concrete}}. \tag{3.28}$$

Herein, their range values are:

- Cast steel longit. resistance/unit length: $R_{z,\,steel} = \frac{1}{\frac{\pi}{4}(d^2-(d-2t)^2)k_{steel}} \sim 80$ [K/(W·m)]
- Concrete longit. resistance/unit length: $R_{z,\,concrete} = \frac{1}{\frac{\pi}{4}(D^2-d^2)k_{concrete}} \sim 1$–$100$ [K/(W·m)]

Thus, at some configurations $R_{z,steel} \sim R_{z,concrete}$, which might conflict with this assumption. However, it is worth noting the high longitudinal conductive resistance, whose values divided by two is not expected to affect the final results. An approximated model for the piping

conduction would be to multiply the concrete axial thermal conductivity by the proper value to include the pipe conductivity in the overall conductivity; this option is not considered herein.

Regarding the steel storage capacity, the ratio of the storage capacity with the pipe included to the storage capacity without it is 0.95. The ratio at the optimal case among the configurations studied herein (shown in Section 3.7) is 0.98. Thus, the steel storage capacity effect on the performance parameters is considered small enough to neglect it.

Fluid laminar flow model versus plug flow model

At a first step, the assessment of the plug flow assumption is studied. A plug flow is a flow with uniform velocity along the tube sectional area. In the laminar flow, a parabolic velocity profile with zero at the tube wall and maximum at the centerline is obtained due to viscosity of the fluid. The conjugated convective heat transfer problem is solved through the conservation of mass for incompressible fluid equation, the Navier-Stokes equation (solar salt is assumed to be a Newtonian fluid), and the energy equation for both the fluid and the solid. No heat generation in the fluid flow due to viscous dissipation is considered. The axisymmetric equations are the mass conservation equation

$$\frac{1}{r}\frac{\partial}{\partial r}(ru_r) + \frac{\partial u_z}{\partial z} = 0, \tag{3.29}$$

the Navier-Stokes radial equation

$$\rho\left(\frac{\partial u_r}{\partial t} + u_r\frac{\partial u_r}{\partial r} + u_z\frac{\partial u_r}{\partial z}\right) = -\frac{\partial p}{\partial r} + \mu\left(\frac{\partial}{\partial r}\left(\frac{1}{r}\frac{\partial}{\partial r}(ru_r)\right) + \frac{\partial^2 u_r}{\partial z^2}\right), \tag{3.30}$$

the Navier-Stokes longitudinal equation,

$$\rho\left(\frac{\partial u_z}{\partial t} + u_r\frac{\partial u_z}{\partial r} + u_z\frac{\partial u_z}{\partial z}\right) = -\frac{\partial p}{\partial z} + \mu\left(\frac{1}{r}\frac{\partial}{\partial r}\left(r\frac{\partial u_z}{\partial r}\right) + \frac{\partial^2 u_z}{\partial z^2}\right), \tag{3.31}$$

the energy equation in the fluid,

$$\rho c_p \left(\frac{\partial T}{\partial t} + u_r \frac{\partial T}{\partial r} + u_z \frac{\partial T}{\partial z} \right) = \frac{k}{r} \frac{\partial}{\partial r} \left(r \frac{\partial T}{\partial r} \right) + k \frac{\partial^2 T}{\partial z^2}, \tag{3.32}$$

and the energy equation in the solid

$$\rho c_p \frac{\partial T}{\partial t} = \frac{k}{r} \frac{\partial}{\partial r} \left(r \frac{\partial T}{\partial r} \right) + k \frac{\partial^2 T}{\partial z^2}. \tag{3.33}$$

The problem is neither hydrodynamically nor thermally fully developed. In this conjugated convective heat transfer problem, another boundary condition and initial condition is added to the model: no-slip condition at the tube wall, and at the initial time velocity is zero in the tube. To avoid numerical artifacts due to conflict between both velocity boundary conditions at the inlet (set to the inlet velocity) and at the wall (no-slip condition), a parabolic profile is imposed for the inlet velocity to satisfy the no-slip wall boundary condition at the point $(r, z) = (d/2, 0)$. Following the same purpose of avoiding numerical artifacts, the conflict between the initial and the boundary condition temperatures and velocity, the inlet temperature and velocity are approximated by a smooth step function, already built in COMSOL. The extent of this smooth step function, 50 s, has negligible effect on the discharge process.

The Nusselt number under constant boundary conditions at hydrodynamically and thermally fully developed flow for the laminar regime and plug flow is shown in Table 3.5.

Herein, the characterization of the Nu_d number for laminar and plug flow under varying boundary conditions is performed. Figure 3-7 shows the Nusselt number value as a function of the absolute difference between the fluid bulk temperature and the wall temperature at a length higher than the entrance length for a $Re_d = 1,000$ under laminar and plug flow with $d = 0.1$ m, $L = 500$ m, and four ϵ values. Nu_d is calculated as described in Section 3.4.2. The CV is located at a length z_{CV} higher than the entrance length. The temperature difference varies during the discharge cycle. At the beginning, it is zero. For some period of time, the temperature difference remains zero, until the HTF that enters at $T_{bulk}(0, t > 0) = T_c$ is

not heated up until T_h at the moment it reaches the CV position. At this point, thermal energy is transfered from the core solid material to the HTF, lowering the temperature of the storage system at the CV point. However, the rate of decrease of the $T_{bulk}(z_{CV}, t)$ is higher than the rate of decrease of the $T_{wall}(z_{CV}, t)$, thus, the temperature difference increases until a maximum. At the maximum, the inflexion point occurs, where the rate of decrease of $T_{bulk}(z_{CV}, t)$ is lower than the rate of decrease of the $T_{wall}(z_{CV}, t)$. After this moment, the temperature difference decreases, approaching zero. In the limit of the temperature difference to zero, Nu_d number goes to infinity and the heat transfer rate from the storage system to the fluid also goes to zero. Figure 3-11 shows a perfect overlap of Nu_d as a function of ΔT for different values of ϵ. ϵ affects the time needed for ΔT to go to zero, that is, the discharge time period $\tau_{discharge}$, but not the actual values that the convective heat transfer coefficient h acquires during the discharge process. It can be seen that Nu_d for plug flow is approximately 1.5 times higher than laminar flow. Thus, the performance analysis under plug flow assumption gives an upper bound performance of the real conjugated problem. However, in order to obtain a more accurate approximation, the thermal conductivity of the solar salt is artificially changed, so that the convective heat transfer coefficient is similar to the laminar flow one. Thus, for this case study, in the plug flow simulations the solar salt thermal conductivity is set to 0.36 W/(m·K). Using this approximation, the plug flow results show a better agreement with the results of the laminar flow model, as shown in Table 3.6. Therein, $\eta_{discharge}$, discharge time $\tau_{discharge}$, and the CPU time is shown for the laminar flow model, the plug flow model without changing k_{HTF}, and plug flow model with k_{HTF} changed to match the convective heat transfer coefficient calculated for the laminar flow model case. The base case comparison is the laminar flow model. It is shown that the computational time is around 40% lower for the plug flow models, and that $\eta_{discharge}$ and $\tau_{discharge}$ are similar for both the laminar flow model and the plug flow model with k_{HTF} changed.

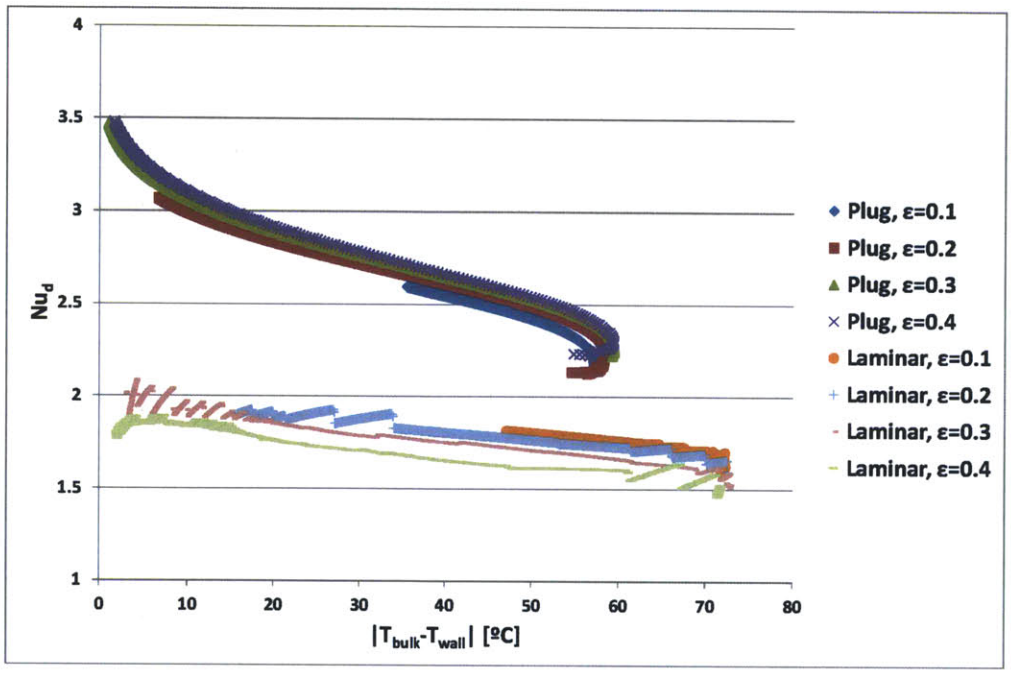

Figure 3-7: $Nu_d - \Delta$T: relation of the Nusselt number versus the absolute difference between the fluid bulk temperature and the wall temperature at a length higher than the entrance length for a $Re_d = 1,000$ under laminar and plug flow for different tube cross sectional area to total storage system cross sectional area, ϵ. The plug flow Nu_d is above the laminar flow Nu_d.

Discharge study versus charge study

Herein, only the discharge process is analyzed. However, since the material properties are independent of temperature, the results from the charge process are exactly the same, assuming the charge process at the same conditions as the discharge process, that is, uniform initial temperature, no heat losses to the ambient, lowest inlet temperature T_c, etc (Section 3.2). Charge time, heat transfer into the storage system, and charge efficiency are calculated analogous as the ones at the discharge process. Charge time period τ_{charge} is calculated as the time period where the non-dimensional bulk outlet temperature $\theta_{bulk}(L,t)$ (monotonically

Table 3.6: Laminar flow versus plug flow results for $Re_d = 1,000$ under plug flow with $d = 0.1$ m, $D = 0.2236$ m, and $L = 500$ m: laminar flow model is the base case for the calculation of the differences in $\eta_{discharge}$, $\tau_{discharge}$, and CPU time

Case study	**Laminar flow**	**Plug flow, k_{HTF}**	**Plug flow, $k_{HTF,changed}$**
$\eta_{discharge}$ [%]	47.7	56.6	50.9
$\eta_{discharge}$ difference [%]	-	15.7	6.3
$\tau_{discharge}$ [h]	16.1	18.7	16.9
$\tau_{discharge}$ difference [%]	-	19.2	4.7
CPU time [s]	811	470	462
CPU time difference [%]	-	42	43

increasing in time) is equal to a certain coefficient θ'_0,

$$\theta_{bulk}(L, \tau_{charge}) = \theta'_0, \tag{3.34}$$

where θ'_0 is set to 0.1. The total thermal energy input the storage system is

$$Q_{input} = \int_0^{\tau_{charge}} \dot{m}_{HTF}(t) c_{p,HTF}(T_h - T_{bulk}(L,t))dt. \tag{3.35}$$

Finally, the charge efficiency is calculated as the ratio of the total thermal energy input during the charge period to the total thermal energy capacity

$$\eta_{charge} = \frac{Q_{input}}{U_{th}}. \tag{3.36}$$

Table 3.7 shows the results for charge and discharge for $d = 0.1$ m, $D = 0.2236$ m, and $L = 500$ m, $Re_d = 1,000$ for no plates and $b = 10\%$ plates added. Herein, a good block performance is not sought. Rather, the purpose of this section is to show that charge and discharge process are analogous and therefore, the parameters calculated in the present study can be extended to the complete charge-discharge cycle, even though only discharging is analyzed.

Table 3.7: Charge and discharge process performance comparison for d = 0.1 m, D = 0.2236 m, and L = 500 m, Re_d = 1,000 for no plates and b = 10% plates added: charge and discharge process are analogous and therefore, the parameters calculated in the present study can be extended to the complete charge-discharge cycle, even though only discharging is analyzed.

Case study	**No plates**	**b = 10% plates**
$\eta_{discharge}$ [%]	56.61	62.46
η_{charge} [%]	56.61	62.46
$\tau_{discharge}$ [h]	18.7	20.6
τ_{charge} [h]	18.7	20.6

Equivalent material properties when the high conductive material is added

At Re_d = 10,000, the storage length L needed to obtain a good efficiency is found to be of the order of 1,000 m for both the plain design (no aluminum added), and the design with heat transfer structures, based on the simulations studied. When adding the high conductive material, the high number of plates (best heat transfer structure arrangement as will be soon in Section 3.5.1) needed to simulate the block makes the problem intractable. In order to obtain an approximation of its performance, the material combination equivalent properties are calculated. Properties ρ, and c_p are calculated as a volume weighted average

$$\rho_{eq} = \rho_{concrete}(1-b) + \rho_{metal}b \tag{3.37}$$

$$c_{p,eq} = c_{p,concrete}(1-b) + c_{p,metal}b, \tag{3.38}$$

where b is the percentage volume of aluminum added. The equivalent longitudinal thermal conductivity is found using the series equivalent thermal resistance equation (3.27),

$$R_z = \frac{1-b}{k_{concrete}\frac{\pi}{4}(D^2-d^2)} + \frac{b}{k_{metal}\frac{\pi}{4}(D^2-d^2)} = \frac{1}{k_{eq}\frac{\pi}{4}(D^2-d^2)}. \tag{3.39}$$

Table 3.8: Equivalent material versus plates performance

	$Re_d = 500$	$Re_d = 1000$
$\eta_{discharge}$ plates modeled [%]	67	54.7
$\eta_{discharge}$ equivalent material [%]	68	56.8
$\eta_{discharge}$ difference [%]	1.5	3.7
$\tau_{discharge}$ plates modeled [h]	29.4	12.1
$\tau_{discharge}$ equivalent material [h]	30.2	12.6
$\tau_{discharge}$ difference [%]	2.6	3.9
CPU time plates modeled [s]	2,105	2,536
CPU time equivalent material [s]	780	950
CPU time difference [%]	63	62.5

The equivalent radial thermal conductivity is found using the parallel equivalent thermal resistance equation (3.28),

$$\frac{1}{R_r} = \frac{2\pi k_{concrete}(1-b)}{\log(D/d)} + \frac{2\pi k_{metal} b}{\log(D/d)} = \frac{2\pi k_{eq} 1}{\log(D/d)}. \tag{3.40}$$

Table 3.8 compares the results for the same block configuration, $d = 0.1$ m, $D = 0.2236$ m, $\epsilon = 0.2$, and $L = 200$ m, under two different operation regimes, $Re_d = 500$, and $Re_d = 1,000$, modeling the plates and concrete separately versus modeling the system using the equivalent material properties. $\tau_{discharge}$ and $\eta_{discharge}$ shows a good agreement. Also, the computational time is significantly lower.

The temperature profiles of the two configurations (plates modeled versus equivalent properties material) is shown in Figure 3-8 for $Re_d = 10,000$, $b = 10\%$, $d = 0.1$ m, $D = 0.4472$ m, $\epsilon = 0.05$, and $L = 60$ m at two different times ($t = 6,000$ s left, and $t = 10,000$ s right). It shows the center line tube temperature (at $r = 0$), the tube wall temperature (at $r = d/2$), and the storage external wall temperature (at $r = D/2$) for the case where the aluminum plates are modeled (colored curves), and the case where equivalent properties are assumed (black

curves overlapping on the others). A good agreement between the two is shown. Looking closer at the tube wall temperature and specially at the storage external wall temperature of the model with the plates, their thickness is higher than the other curves. This feature is explained in detail in Section 3.7.1.

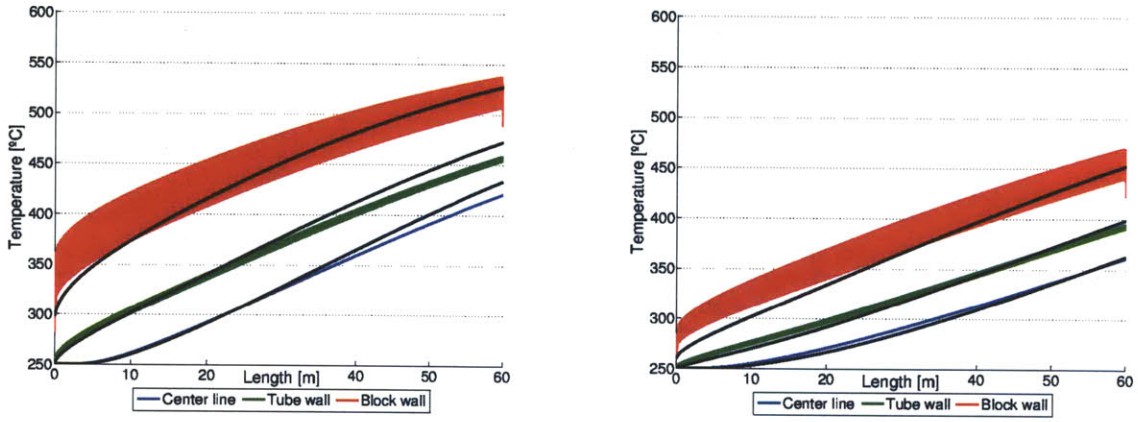

Figure 3-8: Center line tube temperature (at $r = 0$), tube wall temperature (at $r = d/2$), and storage external wall temperature (at $r = D/2$) versus the longitudinal length at $t = 6,000$ s (left) and $t = 10,000$ s (right) after the discharge process started, for $Re_d = 10,000$, $d = 0.1$ m, $D = 0.4472$ m, and $\epsilon = 0.05$. Colored curves are the case study where the plates are modeled, black curves are the case study where the material with equivalent properties is modeled.

3.5 Heat Transfer Structures Design and Turbulent Regime Operation

3.5.1 Heat Transfer Structures: plates versus reinforced bars

The objective of adding the high thermal conductive material is to decrease the thermal resistance of the storage material in the radial direction, without decreasing it significantly in the longitudinal direction. Thus, the more high conductivity material disposed in the radial direction the better. Reinforced bars and fins are reported in literature [8, 27], as well as plates [58]. In the present study, a plate configuration is claimed to be better, since

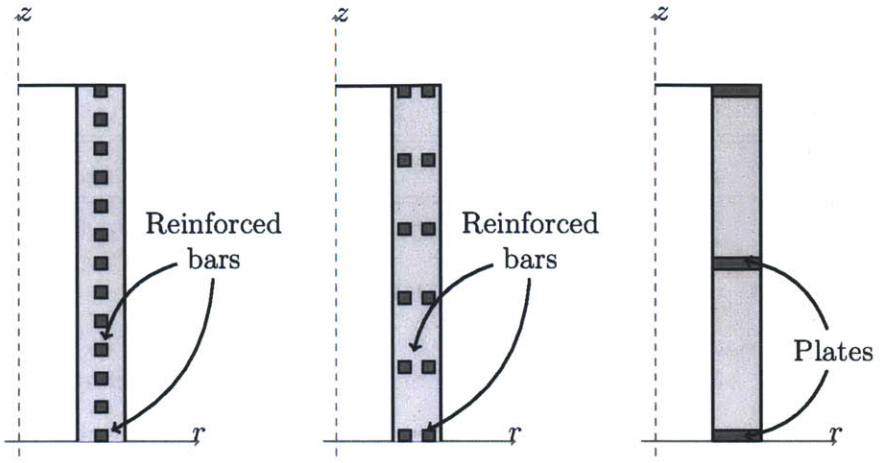

Figure 3-9: Three different distributions of the heat transfer structures with equal amount of added material b = 10%: reinforced bars (i) (left), reinforced bars (ii) (middle), and plates (right)

its arrangement decreases the radial conductive thermal resistance more and increases the longitudinal thermal resistance less than the reinforced bars configuration, by construction.

Three different heat transfer structure configurations with equal amount of added aluminum b = 10% are analyzed (Figure 3-9), for Re_d = 1,000, d = 0.1 m, D = 0.2236 m, ϵ = 0.2, and L = 100 m. In the first configuration, the aluminum is arranged as reinforced bars with only one element at each height in the concrete, (i). In the second configuration, the aluminum is arranged as reinforced bars with two elements at each height in the concrete (ii). Finally, aluminum is added in the form of plates. Plate thickness and side length of the bar are the same, 0.01 m. Table 3.9 shows the results obtained from the simulations. The plate configuration accounts for an $\eta_{discharge}$ of 46.24%, versus the 44% of the reinforced bar configuration (i), and 43.29% of the reinforced bar configuration (ii). Although the efficiencies are low since the storage length is far from optimal, it is seen that the plate configuration is favorable, confirming the theory.

Table 3.9: Results for three different distributions of the heat transfer structures with equal amount of added material $b = 10\%$: reinforced bars (i), reinforced bars (ii), and plates

Configuration	Reinforced bar (i)	Reinforced bar (ii)	Plate
$\eta_{discharge}$	43.29%	44%	46.24%

3.5.2 Turbulent Regime Operation Model

The advantage of adding plates to the thermal storage is the decrease in the radial conduction thermal resistance. However, the convective thermal resistance has also to be taken into account. Due to the solar salt low thermal conductivity, the convective thermal resistance is significant. In order to lower this value, the HTF flow operates in the turbulent regime. The onset of the turbulent regime happens at a Reynolds number of 10,000. Nusselt number in the turbulent regime is based on the Gnielinski experimental relation, where the friction factor is calculated with Petuchov's formula [38]:

$$\text{Petuchov's}, f = (0.790 \log Re_d - 1.64)^{-2} \tag{3.41}$$

$$\text{Gnielinski's}, Nu_d = \frac{(f/8)(Re_d - 1000)Pr}{1 + 12.7(f/8)^{1/2}(Pr^{2/3} - 1)} \tag{3.42}$$

Based on equations (3.41) and (3.42), the $Nu_d - Re_d$ curve's slope is lower than one at any point and decreases with Re_d (Figure 3-10). Thus, at a fixed tube diameter d, as Re_d increases, Nu_d increases at a rate lower than linearly at the turbulent regime. Also, at a fixed tube diameter d, as Re_d increases, the HTF mass flow rate $\dot{m}_{HTF}$ which needs to be heated up, increases linearly. Thus, as Re_d increases, $\dot{m}_{HTF}$ increases more than the convective heat transfer coefficient h. Since the discharge process is heat transfer limited, the maximum benefit of the convective thermal resistance decrease in discharge efficiency terms occurs at the onset of the turbulent regime Re_d. That is, at $Re_d = 10,000$.

In order to approximate the turbulent regime flow by a plug flow model, the HTF thermal conductivity is artificially increased so that the heat transfer convective coefficient matches the turbulent regime value calculated with equations (3.41) and (3.42), since the heat transfer

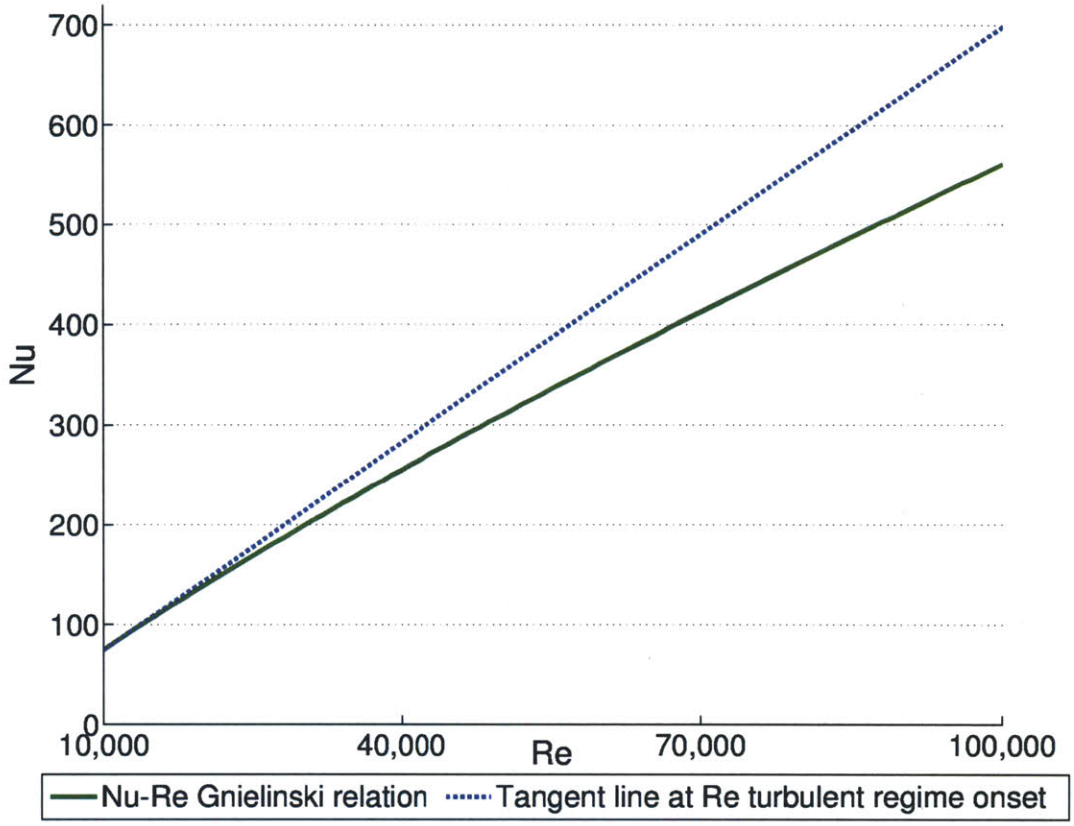

Figure 3-10: Nu_d–Re_d turbulent regime relation: solid green line shows the Nusselt-Reynolds Gnielinski experimental relation where the friction factor is calculated based on Petuchov's relation, dashed blue line shows the tangent line at the onset turbulent regime Reynolds number, 10,000. This plot shows that the steepest slope of this relation is at the onset turbulent regime Reynolds number, 10,000, and that this slope is lower than one.

convective coefficient is independent of the boundary conditions. Figure 3-11 shows the Nusselt number as a function of the absolute difference between the fluid bulk temperature and the wall temperature for a Re_d = 10,000 under plug flow with d = 0.1 m. Nu_d is calculated as described in Section 3.4.2. The CV is located at a length z_{CV} higher than the entrance length. The temperature difference varies during the discharge cycle. At the beginning, it is zero. For some period of time, the temperature difference remains zero, until the HTF that enters at $T_{bulk}(0,t) = T_c$ is not heated up until T_h at the moment it reaches

the CV position. At this point, thermal energy is transfered from the core solid material to the HTF, lowering the temperature of the storage system at the CV point. However, the rate of decrease of the $T_{bulk}(z_{CV}, t)$ is higher than the rate of decrease of the $T_{wall}(z_{CV}, t)$, thus, the temperature difference increases until a maximum. At the maximum, the inflexion point occurs, where the rate of decrease of $T_{bulk}(z_{CV}, t)$ is lower than the rate of decrease of the $T_{wall}(z_{CV}, t)$. After this moment, the temperature difference decreases, approaching zero. In the limit of the temperature difference to zero, Nu_d number goes to infinity and the heat transfer rate from the storage system to the fluid also goes to zero. Figure 3-11 shows a perfect overlap of Nu_d as a function of ΔT for different values of ϵ. ϵ affects the time needed for ΔT to go to zero, that is, the discharge time period $\tau_{discharge}$, but not the actual values that the convective heat transfer coefficient h acquires during the discharge process. Figure 3-12 shows the case for the case with d = 0.05 m.

For d = 0.1 m, the averaged Nusselt number $\bar{N}u_d$ is considered equal to 2.75. At Re_d = 10,000 and under turbulent regime, using equations (3.41) and (3.42), the theoretical heat transfer convective coefficient in the turbulent regime is equal to 405.6 W/(m^2·K). Thus, in the plug flow simulations the solar salt thermal conductivity is set to 15 W/(m·K). For d = 0.05 m, following the same procedure, solar salt thermal conductivity is set to 30 W/(m·K)

3.6 Cost Calculation

In order to calculate the cost of the thermal energy storage system, the materials and the parasitic losses from the pumping power are taken into account. The materials used are the matrix material, the high thermal conductivity material, the piping material, and the heat transfer fluid. Pumping power to account for the pressure drop is considered. Herein, the pressure drop is calculated analytically from the Darcy friction factor f_d:

$$\Delta p = f_d \frac{L}{d} \rho_{HTF} \frac{\bar{u}_z^2}{2}. \tag{3.43}$$

The Darcy friction factor depends on the flow regime:

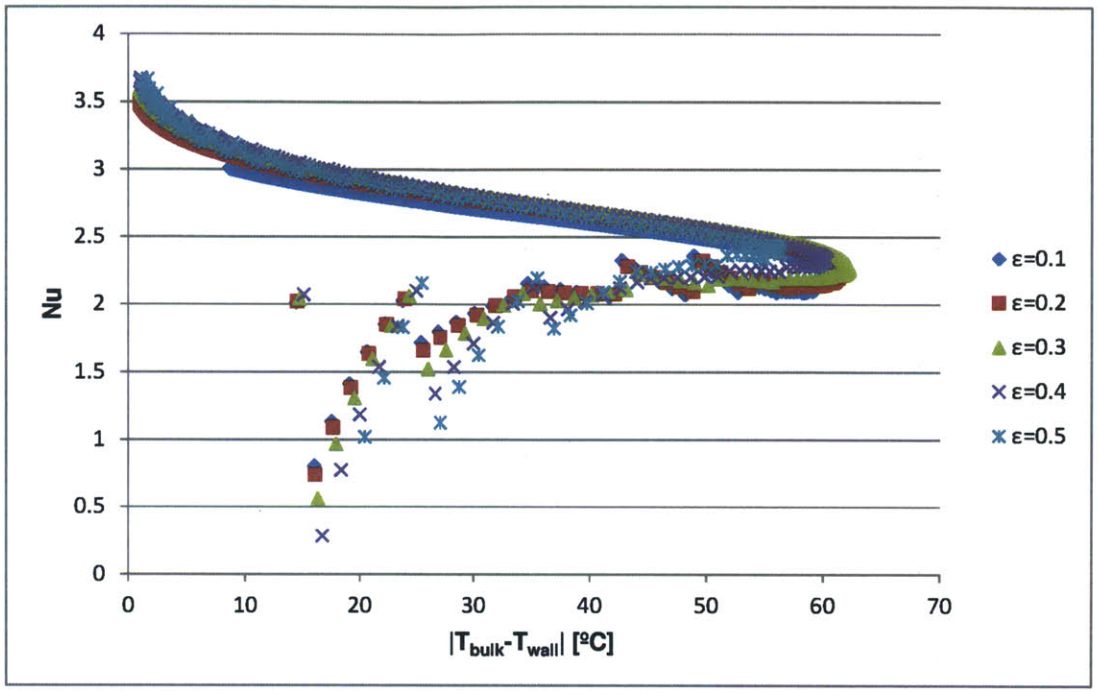

Figure 3-11: $Nu_d - \Delta T$: relation of the Nusselt number versus the absolute difference between the fluid bulk temperature and the wall temperature at a length higher than the entrance length for a Re_d = 10,000 and d = 0.1 m under plug flow for different tube cross sectional area to total storage system cross sectional area, ϵ.

$$\text{Laminar } (Re_d < 2,300)\text{: } f_d = \frac{64}{Re_d} \tag{3.44}$$

$$\text{Turbulent } (Re_d > 10,000)\text{: Petuchov's, } f_d = (0.790 \log Re_d - 1.64)^{-2} \tag{3.45}$$

The electric power consumed by the pump is calculated by

$$\dot{W}_{pump} = \Delta p \cdot \bar{u}_z \frac{\pi}{4} d^2 \frac{1}{\eta_{pump}}, \tag{3.46}$$

where η_{pump} is the pump isentropic efficiency. The electric energy consumed by the pump is

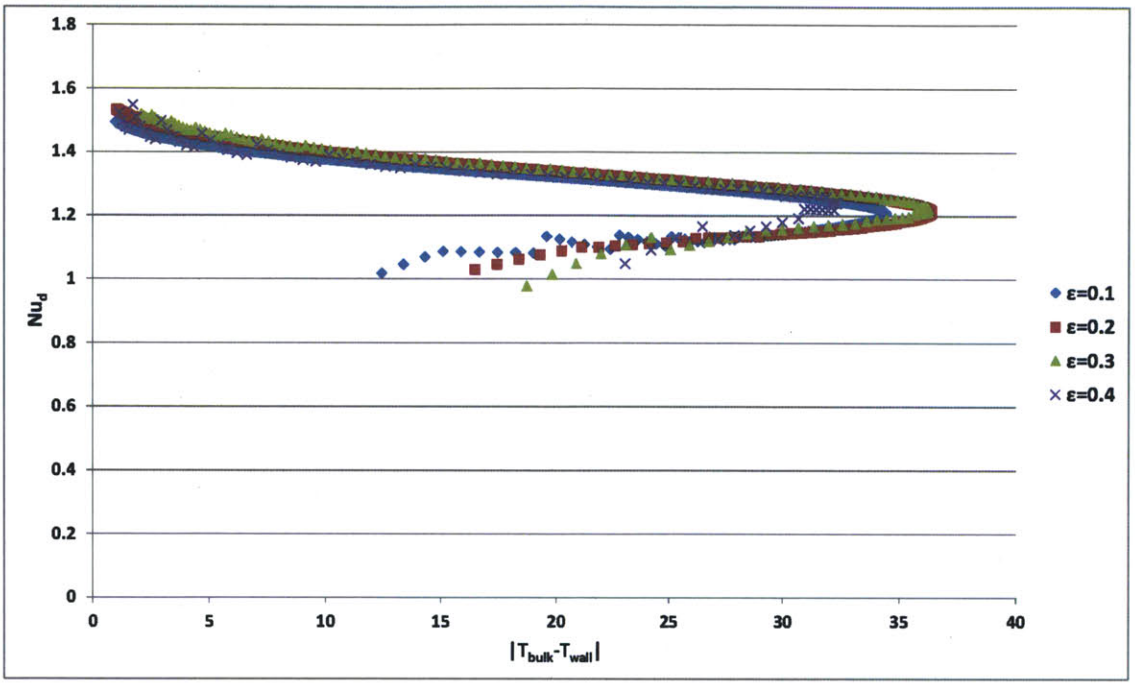

Figure 3-12: $Nu_d - \Delta$T: relation of the Nusselt number versus the absolute difference between the fluid bulk temperature and the wall temperature at a length higher than the entrance length for a Re_d = 10,000 and d = 0.05 m under plug flow for different tube cross sectional area to total storage system cross sectional area, ϵ.

calculated by

$$E_{pump} = \dot{W}_{pump}\tau. \tag{3.47}$$

The economic impact of the pressure drop is calculated by

$$Cost_{pump} = E_{pump} \cdot \bar{c}, \tag{3.48}$$

where $\bar{c}$ is a representative constant electricity price, assumed 0.05 \$/kWh herein to estimate the cost within an order of magnitude. Molten salt pumps are quite inefficient, of the order of 45% at best [11]. Herein, 40% efficiency is considered.

Thus, the total cost of each storage block is calculated by

$$Cost_{block} = Cost_{pump} + Cost_{concrete} + Cost_{pipe} + Cost_{metal} + Cost_{HTF}. \quad (3.49)$$

3.7 Results of the Discharge Process for Different Storage Configurations

Herein, the study is focused on a thermal storage system to overcome the hourly variability nature of the incoming solar energy in a solar-thermal power plant. That is, a daily time scale with 24-hour operation cycles is considered. Thus, a discharge time lower than 12 hours is needed. Also, a high discharge efficiency is sought.

First, a qualitatively analysis of the convective and conductive thermal resistances of the storage system for laminar and turbulent regimes, and for the plain design and with heat transfer structures added is shown. Later, a more rigorous analysis of different configurations, designs, and operation regimes is presented. Therein, two different tube diameters d = 0.1 m, and d = 0.05 m, based on [11, 6], are considered. Firstly, laminar operation regime is analyzed through two Reynolds numbers, Re_d = 500, and Re_d = 1,000, for two different material configurations: (i) plain design without heat transfer structures added, (ii) b = 10% aluminum plates added. The calculated performance parameters show that this operation strategy is not useful for the application sought herein. Secondly, the thermal energy storage system is analyzed under turbulent regime operation at Re_d = 10,000 (Section 3.5.2) for four different material configurations: (i) plain design without heat transfer structures added, (ii) b = 5% aluminum plates added, (iii) b = 10% aluminum plates added, and (iv) b = 20% aluminum plates added. Under these configurations, a number of case studies with different storage system length L, and ratio of tube cross sectional area to block cross sectional ϵ, which determines the block external diameter D, are analyzed. In the following results the case studies are referred by the numbers in Table 3.10.

Table 3.10: Case study numbering for d = 0.1 m

Case study	Re_d =500, 1000				Re_d = 10,000			
			d = 0.1 m	d = 0.05 m			d = 0.1 m	d = 0.05 m
-	L [m]	ϵ	D [m]	D [m]	L [m]	ϵ	D [m]	D [m]
1	50	0.01	1	0.5	500	0.01	1	0.5
2	100	0.01	1	0.5	1000	0.01	1	0.5
3	150	0.01	1	0.5	2000	0.01	1	0.5
4	200	0.01	1	0.5	3000	0.01	1	0.5
5	300	0.01	1	0.5	5000	0.01	1	0.5
6	400	0.01	1	0.5	7000	0.01	1	0.5
7	500	0.01	1	0.5	8000	0.01	1	0.5
8	600	0.01	1	0.5	9000	0.01	1	0.5
9	50	0.05	0.4472	0.2236	500	0.05	0.4472	0.2236
10	100	0.05	0.4472	0.2236	1000	0.05	0.4472	0.2236
11	150	0.05	0.4472	0.2236	2000	0.05	0.4472	0.2236
12	200	0.05	0.4472	0.2236	3000	0.05	0.4472	0.2236
13	300	0.05	0.4472	0.2236	5000	0.05	0.4472	0.2236
14	400	0.05	0.4472	0.2236	7000	0.05	0.4472	0.2236
15	500	0.05	0.4472	0.2236	8000	0.05	0.4472	0.2236
16	600	0.05	0.4472	0.2236	9000	0.05	0.4472	0.2236
17	50	0.1	0.3162	0.1581	500	0.1	0.3162	0.1581
18	100	0.1	0.3162	0.1581	1000	0.1	0.3162	0.1581
19	150	0.1	0.3162	0.1581	2000	0.1	0.3162	0.1581
20	200	0.1	0.3162	0.1581	3000	0.1	0.3162	0.1581
21	300	0.1	0.3162	0.1581	5000	0.1	0.3162	0.1581
22	400	0.1	0.3162	0.1581	7000	0.1	0.3162	0.1581
23	500	0.1	0.3162	0.1581	8000	0.1	0.3162	0.1581
24	600	0.1	0.3162	0.1581	9000	0.1	0.3162	0.1581
25	50	0.2	0.2236	0.1118	500	0.2	0.2236	0.1118
26	100	0.2	0.2236	0.1118	1000	0.2	0.2236	0.1118
27	150	0.2	0.2236	0.1118	2000	0.2	0.2236	0.1118
28	200	0.2	0.2236	0.1118	3000	0.2	0.2236	0.1118
29	300	0.2	0.2236	0.1118	5000	0.2	0.2236	0.1118
30	400	0.2	0.2236	0.1118	7000	0.2	0.2236	0.1118
31	500	0.2	0.2236	0.1118	8000	0.2	0.2236	0.1118
32	600	0.2	0.2236	0.1118	9000	0.2	0.2236	0.1118
33	50	0.3	0.1826	0.0913	500	0.3	0.1826	0.0913
34	100	0.3	0.1826	0.0913	1000	0.3	0.1826	0.0913
35	150	0.3	0.1826	0.0913	2000	0.3	0.1826	0.0913
36	200	0.3	0.1826	0.0913	3000	0.3	0.1826	0.0913
37	300	0.3	0.1826	0.0913	5000	0.3	0.1826	0.0913
38	400	0.3	0.1826	0.0913	7000	0.3	0.1826	0.0913
39	500	0.3	0.1826	0.0913	8000	0.3	0.1826	0.0913
40	600	0.3	0.1826	0.0913	9000	0.3	0.1826	0.0913
41	50	0.4	0.1581	0.0791	500	0.4	0.1581	0.0791
42	100	0.4	0.1581	0.0791	1000	0.4	0.1581	0.0791
43	150	0.4	0.1581	0.0791	2000	0.4	0.1581	0.0791
44	200	0.4	0.1581	0.0791	3000	0.4	0.1581	0.0791
45	300	0.4	0.1581	0.0791	5000	0.4	0.1581	0.0791
46	400	0.4	0.1581	0.0791	7000	0.4	0.1581	0.0791
47	500	0.4	0.1581	0.0791	8000	0.4	0.1581	0.0791
48	600	0.4	0.1581	0.0791	9000	0.4	0.1581	0.0791
49	50	0.5	0.1414	0.0707	500	0.5	0.1414	0.0707
50	100	0.5	0.1414	0.0707	1000	0.5	0.1414	0.0707
51	150	0.5	0.1414	0.0707	2000	0.5	0.1414	0.0707
52	200	0.5	0.1414	0.0707	3000	0.5	0.1414	0.0707
53	300	0.5	0.1414	0.0707	5000	0.5	0.1414	0.0707
54	400	0.5	0.1414	0.0707	7000	0.5	0.1414	0.0707
55	500	0.5	0.1414	0.0707	8000	0.5	0.1414	0.0707
56	600	0.5	0.1414	0.0707	9000	0.5	0.1414	0.0707

3.7.1 Qualitatively analysis of the conductive and convective thermal resistances

Figures 3-13 to 3-15 reflect the radial conductive and convective thermal resistances, for laminar and turbulent regimes, and for configurations where the storage has plates of thickness δ_{plate} = 0.01 m added as in Figure 3-3, and without them. The block dimensions are d = 0.1 m, D = 0.4472 m, and ϵ = 0.05. Therein, the center line tube temperature (at r = 0), the tube wall temperature (at $r = d/2$), and the storage external wall temperature (at $r = D/2$) is shown versus the longitudinal length at a certain time during the discharge process. Figure 3-13 shows the laminar regime case with Re_d = 1,000 after t = 10,000 s, without and with b = 10% aluminum. It is clear that the plates decrease the conductive thermal resistance in a significant amount. However, the heat transfer is still limited by the high thermal convective resistance of the flow. The latter is decreased in the turbulent regime at Re_d = 10,000, shown in Figure 3-15 at t = 6,000 s. Figure 3-14 zooms in the laminar case with plates added, showing the details of the temperature profile: where the plates exist (marks at z =8.012, 10.015, 12.18 m), the difference between the tube wall temperature and the storage external wall temperature is significantly lower than in the regions fulfill with concrete. This difference is even higher in the Re_d = 10,000 case. The conclusions extracted from this plots with this configuration are the following:

- In the laminar regime for the plain design (no heat transfer structures added), the conductive and convective thermal resistance are similar in magnitude.

- In the laminar regime with b = 10% aluminum added, the convective thermal resistance is higher than the conductive thermal resistance, being the factor that limits the heat transfer.

- In the turbulent regime for the plain design (no heat transfer structures added), the conductive thermal resistance is much larger than the convective thermal resistance, that is, the conductive thermal resistance dominates the convective one.

- In the turbulent regime with b = 10% aluminum added, the conductive and convective thermal resistance are similar in magnitude. A separate analysis shows that the magnitude of these thermal resistances is lower than in the laminar with plain design case.

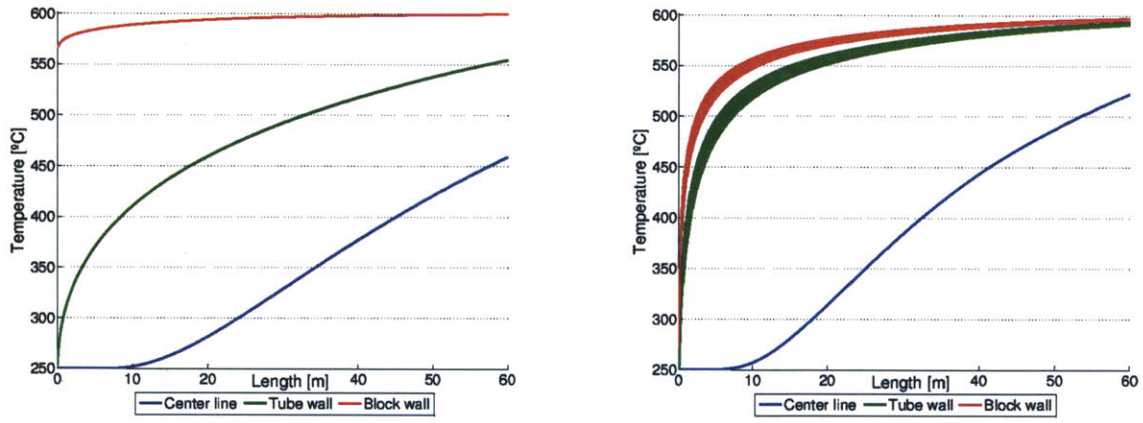

Figure 3-13: Center line tube temperature (at r=0), tube wall temperature (at r=d/2), and storage external wall temperature (at r=D/2) versus the longitudinal length at t = 10,000 s after the discharge process started, for laminar regime (Re_d = 1,000), d = 0.1 m, D = 0.4472 m, and ϵ = 0.05 without (left) and with (right) b = 10% aluminum plates with δ_{plate} = 0.01 m. Where the plates exist (right) the difference between the tube wall temperature and the storage external wall temperature is significantly lower than in the regions fulfill with concrete (see Figure 3-14).

3.7.2 Laminar regime operation

Two different studies in the laminar regime are analyzed (Re_d = 500, and Re_d = 1,000) for two different material configurations: (i) without heat transfer structures added, (ii) b = 10% aluminum plates added. Under these configurations, a number of case studies with different storage system length L, and ratio of tube cross sectional area to block cross sectional ϵ, which determines the block external diameter D, are analyzed.

The discharge efficiency for a constant tube diameter d = 0.1 m versus the storage system length for the cases where aluminum is added are shown on the left of Figures 3-16 and

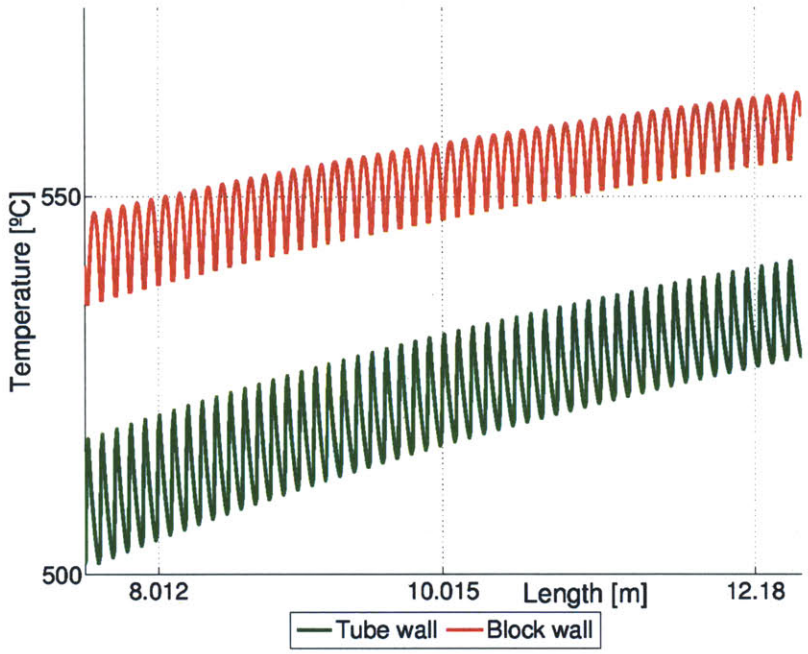

Figure 3-14: Zoomed in of (right) Figure 3-13 shows the temperature profile details: where the plates exist (marks at z =8.012, 10.015, 12.18 m), the difference between the tube wall temperature and the storage external wall temperature is significantly lower than in the regions fulfill with concrete.

3-17 for $Re_d = 500$ and $Re_d = 1,000$, respectively. The discharge efficiency difference between the case of aluminum added minus the discharge efficiency of the case of no plates added is shown on the right. The discharge efficiency as the length L of the storage system increases, because the relative value of the length where the temperature of the HTF changes from T_c to T_h to the total length of the system L decreases. Also, as the thickness of the thermal storage decreases (D decreases, ϵ increases), the efficiency increases since the conductive thermal resistance decreases. Furthermore, it is shown that the effect of adding heat transfer structures is higher when ϵ is lower (D higher). This is expected, since from equation (3.40), the decrease in the equivalent thermal resistance is higher when ϵ is lower (D higher).

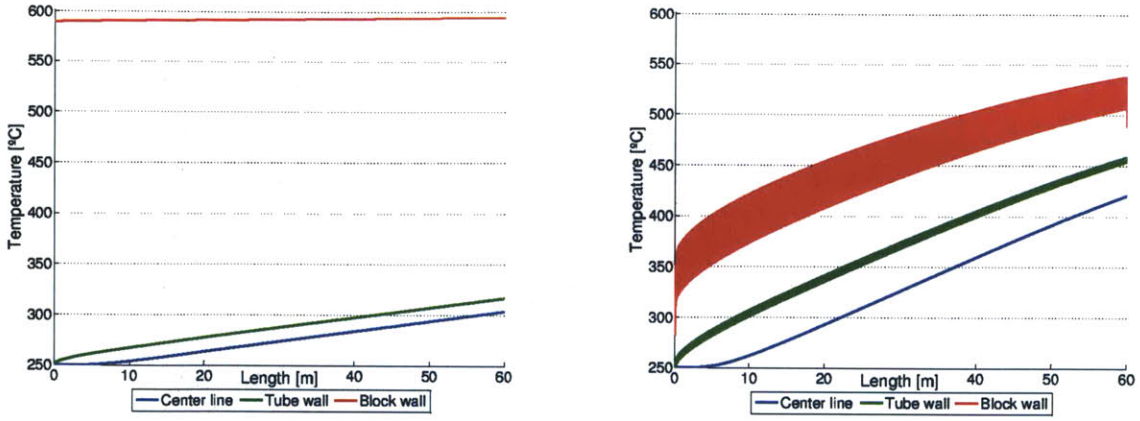

Figure 3-15: Center line tube temperature (at r=0), tube wall temperature (at r=d/2), and storage external wall temperature (at r=D/2) versus the longitudinal length at t = 6,000 s after the discharge process started, for turbulent regime (Re_d = 10,000), d = 0.1 m, D = 0.4472 m, and ϵ = 0.05 without (left) and with (right) b = 10% aluminum plates with δ_{plate} = 0.01 m. Where the plates exist (right) the difference between the tube wall temperature and the storage external wall temperature is significantly lower than in the regions fulfill with concrete (see Figure 3-14).

For each case study, the storage cost $\bar{C}$ [\$/kWh$_t$] is calculated by

$$\bar{C} = \frac{Cost_{block}}{Q_{output}}, \tag{3.50}$$

where $Cost_{block}$ is calculated by equation (3.49), and Q_{output} by equation (3.10). The materials used (matrix material, heat transfer structures, heat transfer fluid, and piping) and the pumping power are considered. As stated above, the storage desirable characteristics are high efficiency, and discharge time lower than 12 hours. Figure 3-18 shows the storage cost [\$/kWh$_t$] versus discharge time and efficiency, for the case studies where heat transfer structures are added with tube diameter d = 0.1 m. In the left, it can be seen that as the length increases, the efficiency increases. In order to filter the results, a discharge time period lower or equal than 12 hours and a efficiency higher or equal than 0.8 is required as a first estimate. These lines are plotted in the graphs. It can be seen that none of the laminar regime case studies passes this filter.

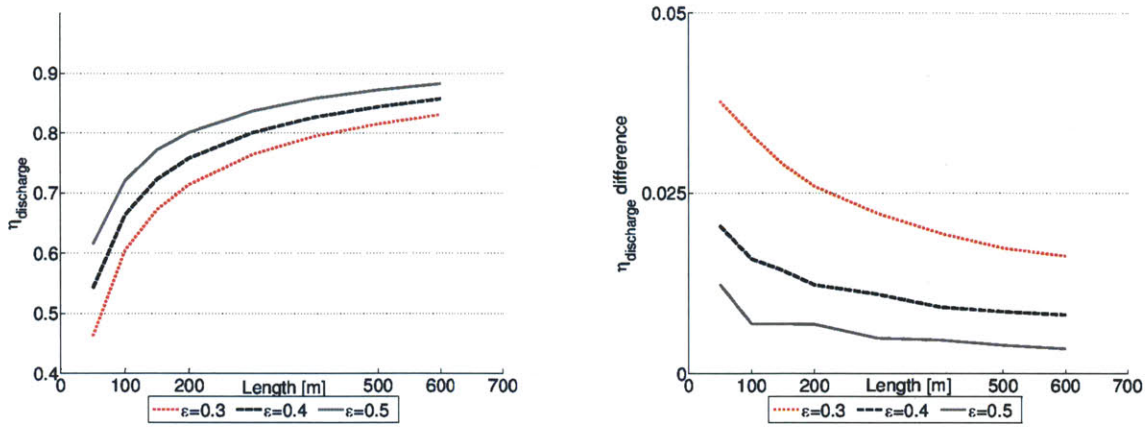

Figure 3-16: Discharge efficiency versus storage length for different ϵ with b = 10% plates added (left), and discharge efficiency difference between the plates case and the no-plates case (right) for Re_d = 500

3.7.3 Turbulent regime operation

Herein, the thermal energy storage system is analyzed under turbulent regime operation at Re_d = 10,000 (Section 3.5.2) for four different material configurations: (i) without heat transfer structures added, (ii) b = 5% aluminum plates added, (iii) b = 10% aluminum plates added, and (iv) b = 20% aluminum plates added. Under these configurations, a number of case studies with different storage system length L, and ratio of tube cross sectional area to block cross sectional area ϵ, which determines the block external diameter D, are analyzed. Table 3.10 enumerates them. This notation is used in the section's plots to indicate each case study.

The discharge efficiency for d = 0.1 m versus the storage system length for the cases with b = 5%, b = 10% and b = 20% of aluminum added are shown on the left of Figures 3-19, 3-20 and 3-21, respectively. On the right of these Figures, the discharge efficiency difference between the case of aluminum added minus the discharge efficiency of the case of no plates added is shown. As in the previous section, the effect of adding heat transfer structures is higher when ϵ is lower (D higher). It is shown that adding heat transfer structures is more beneficial at the turbulent regime. Again, this is expected based on the relative values of

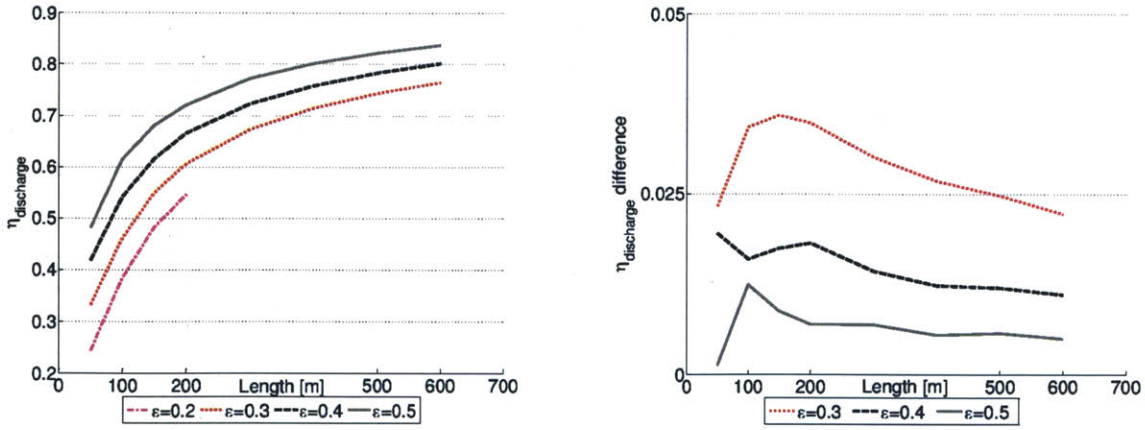

Figure 3-17: Discharge efficiency versus storage length for different ϵ with b = 10% plates added (left), and discharge efficiency difference between the plates case and the no-plates case (right) for $Re_d = 1,000$

conductive and convective thermal resistances. In the laminar regime, the convective thermal resistance has about the same order of magnitude as the conductive one:

- Conductive radial resistance by unit length: $R_r \sim 10^{-2} - 10^{-1}$[(K·m)/W]
- Convective resistance by unit length: $R_h \sim 10^{-1}$[(K·m)/W]]

Thus, although the conductive thermal resistance is decreased by adding the heat transfer structures, the performance does not improve as much because the convective thermal resistance is still limiting the heat transfer. However, in the turbulent regime the convective thermal resistance is decreased significantly , $R_h \sim 8 \cdot 10^{-3}$[K·m)/W]. Thus, the conductive thermal resistance becomes the dominant factor for the heat transfer process, and its decrease after adding the heat transfer structures affects significantly the thermal energy storage system performance. Also, from equation (3.40), the highest decrease in the radial conductive thermal resistance occurs between the no plates added case and the b = 5% of aluminum plates added. This difference is lower from b = 5% to b = 10%, and even lower from b = 10% to b = 20%. This feature can be seen in the results, where no significant difference can be found between the right plots of Figures 3-19 to 3-21. Results are similar for tube diameter d = 0.05 m.

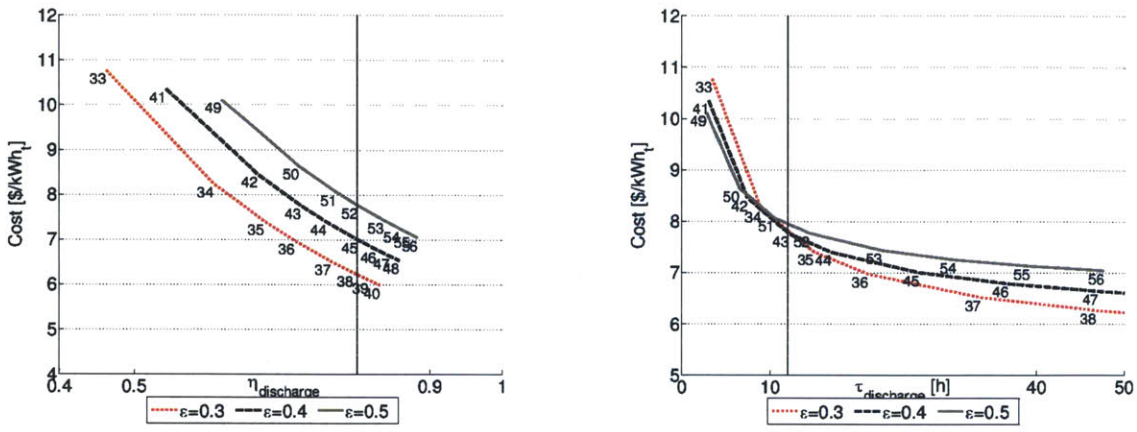

Figure 3-18: Storage cost [$/kWh$_t$] versus discharge efficiency (left) and discharge time (right) for the b = 10% plates added case studies at Re_d = 500 for d = 0.1 m. Numbers are referred to Table 3.10.

For each case study, the storage cost $\bar{C}$ [$/kWh$_t$] is calculated. As stated above, the storage desirable characteristics are high efficiency, and discharge time lower than 12 hours. Figure 3-22 shows the storage cost $\bar{C}$ [$/kWh$_t$] versus discharge time and efficiency, for the case studies where heat transfer structures are added with tube diameter d = 0.1 m and b = 10%. A better performance than in the laminar case can be seen.

For a fixed ϵ, as the storage length L increases, the discharge time also increases, becoming the limiting factor for the storage system, as shown in Figure 3-22 (right). Also, as L increases, $\eta_{discharge}$ increases, as shown in Figure 3-22 (left). For a fixed L, as ϵ increase, $\tau_{discharge}$ decreases and $\eta_{discharge}$ increases. The addition of heat transfer structures to the storage system increases $\eta_{discharge}$ (pushes the curves of Figure 3-22 (left) to the right), and also decreases $\tau_{discharge}$ (pushes the curves of Figure 3-22 (left) to the left). That is, from a thermal storage performance, its addition has only positive effects. Again, in order to filter the results, a discharge time period lower or equal than 12 hours and a efficiency higher or equal than 0.8 is required. These lines are plotted in the graphs. The configurations that satisfy both conditions are, for d = 0.1 m, b = 0% 43, 51, and 52; b = 5% 34, 42, 43, 50, and 51; b = 10% 26, 34, 42, 43, 50, and 51; and the same for b = 20% (26, 34, 42, 43, 50, and 51). Looking at Table 3.10, it can be seen that the suitable storage length L is between 1,000 and

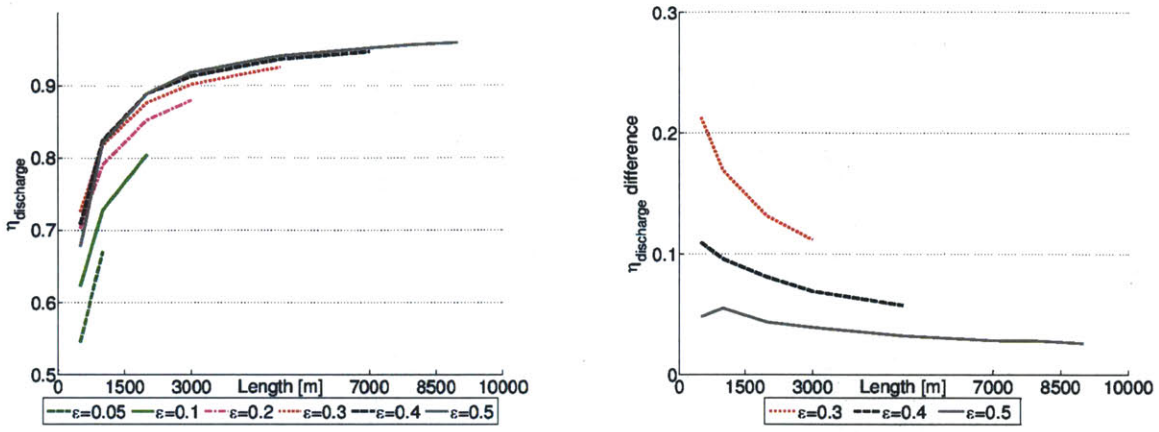

Figure 3-19: Discharge efficiency versus storage length for different ϵ with b = 5% plates added (left), and discharge efficiency difference between the b = 5% plates case and the no-plates case (right) for $Re_d = 10,000$, $d = 0.1$ m

2,000 m. As b increases, more storage configurations pass the filter. For the tube diameter $d = 0.05$ m, the configurations that pass the filter are b = 0% 35, 36, 43, 44, 51, 52, and 53; b = 5% 18, 26, 27, 35, 36, 43, 44, 51, 52, and 53; the same for b = 10% (18, 26, 27, 35, 36, 43, 44, 51, 52, and 53); and for b = 20% 9, 17, 18, 26, 27, 35, 36, 43, 44, 51, 52, and 53. In this case, the appropriate storage lengths is around 2,000 and 3,000 m. It is higher due to the higher inlet velocity (same Re_d for half tube diameter). To do a finer filter, configurations with $\eta_{discharge} \geq 0.9$ is sought. No configuration satisfies these conditions for $d = 0.1$ m. For $d = 0.05$ m, b = 0% 53; b = 5% 36, and 53; same for b = 10% (36, and 53); and for b = 20% 27, 36, and 53. Figure 3-23 shows these case studies in a 3D plot where storage cost $\bar{C}$ is in the z axes, discharge time $\eta_{discharge}$ is in the y axis, and discharge efficiency $\eta_{discharge}$ is in the x axes. The amount of aluminum added is differentiated by the color. The case numbers are labeled next to each point. Case study 36 for b = 5% has the lowest storage cost, 6.691 \$/kWh$_t$ (optimal $\bar{C}$). Case study 27 for b = 20% has the lowest discharge time, 9.8 h (optimal $\tau_{discharge}$). Case study 53 for b = 20% has the highest efficiency with 92.15% (optimal $\eta_{discharge}$). Table 3.11 shows the characteristic of the three configurations. Within the three, the highest $\eta_{discharge}$ has the highest L, and lowest ϵ, whereas the lowest $\tau_{discharge}$ has the lowest L and the highest ϵ. Also, both have the highest percentage of heat transfer

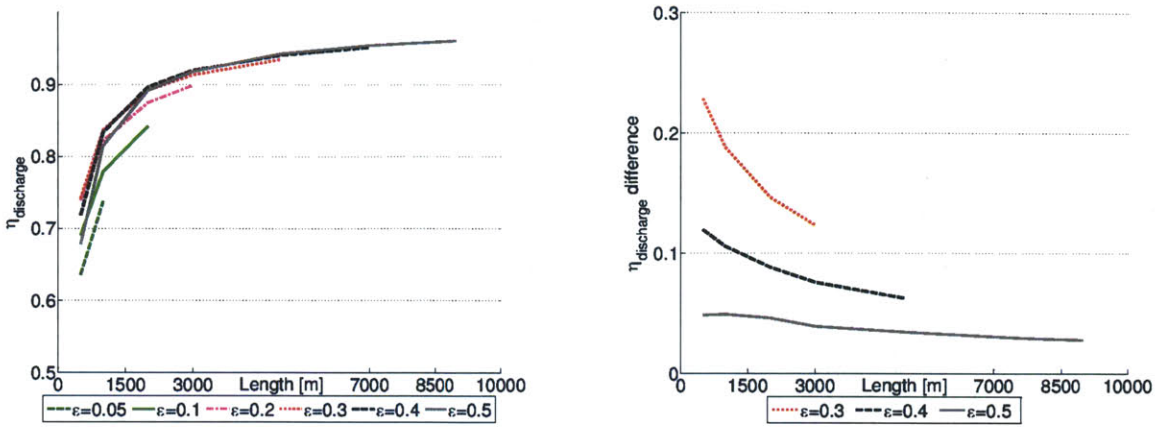

Figure 3-20: Discharge efficiency versus storage length for different ϵ with b = 10% plates added (left), and discharge efficiency difference between the b = 10% plates case and the no-plates case (right) for $Re_d = 10,000$, $d = 0.1$ m

structures studied, $b = 20\%$. The option with the lowest cost is in between the latter two in terms of $\eta_{discharge}$, $\tau_{discharge}$, L, and ϵ.

Finally, the Pareto frontier is shown in Figure 3-24 in 3-dimensions, and in Figures 3-25 to 3-27 in the projection planes. It is shown that points (a), (b), and (c) have among the best combinations of low storage cost, low discharge time, and high efficiency within the configuration analyzed for the application consider herein.

3.7.4 Comparison with other TES

Values in the range of 25 \$/kWh$_t$ to 40 \$/kWh$_t$ are reported for concrete [20], whereas a two-tank nitrate salt energy storage system costs approximately 31 \$/kWh$_t$ [48] to 35 \$/kWh$_t$ [20].

The quantity of solar salt required is for optimal $\bar{C}$ 2.38 kg/kWh$_t$, for optimal $\tau_{discharge}$ 1.61 kg/kWh$_t$, and for optimal $\eta_{discharge}$ 3.83 kg/kWh$_t$. In a two-tank nitrate salt thermal energy storage system, the amount of salt per kWh$_t$ needed for the same operating temperatures is approximately 6.64 kg/kWh$_t$. In the CSPonD concept the amount of salt is about 7.745 kWh$_t$. Thus, although the quantity is substantially smaller than in two-tank systems,

Table 3.11: Principal features of the optimal case study found: lowest $\bar{C}$, (a); lowest $\tau_{discharge}$ (b); and highest $\eta_{discharge}$ (c). (a), (b), and (c) are used to represent these points in the Pareto frontier, Firgures 3-24 to 3-27

Case study	**Lowest $\bar{C}$, 36 (a)**	**Lowest $\tau_{discharge}$, 27 (b)**	**Highest $\eta_{discharge}$, 53 (c)**
$\bar{C}$ [\$/kWh$_{th}$]	6.7	8.5	11.5
$\eta_{discharge}$ [%]	90.52	90.3	92.15
$\tau_{discharge}$ [h]	10	9.8	10.4
d [m]	0.05	0.05	0.05
b [%]	5	20	20
L [m]	3,000	2,000	5,000
D [m]	0.0913	0.1118	0.0707
ϵ	0.3	0.2	0.5
U_{th} [MWh$_t$]	4.9	4.83	5
Q_{output} [MWh$_t$]	4.43	4.36	4.6
$\dot{Q}$ [kW]	447	447	447
Cost concrete [\$]	1,500	1,400	883
Cost aluminum [\$]	4,300	19,500	12,000
Cost salt [\$]	5,200	3,450	8,600
Cost piping [\$]	18,700	12,500	31,200
Cost pumping [\$]	0	0	0
Total cost [\$]	29,700	36,850	52,700

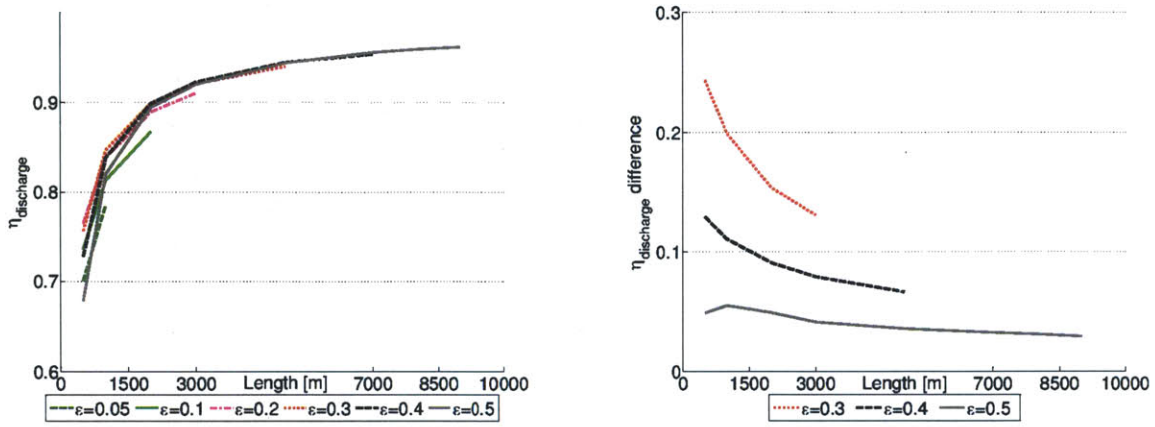

Figure 3-21: Discharge efficiency versus storage length for different ϵ with$b$ = 20% plates added (left), and discharge efficiency difference between the b = 20% plates case and the no-plates case (right) for $Re_d = 10,000$, $d = 0.1$ m

the storage system still needs big quantities of HTF.

3.8 Conclusions

In the presented work, a regenerator type thermal storage system is analyzed in terms of discharge efficiency, discharge time period, and storage cost. Two different tube diameters $d = 0.1$ m, and $d = 0.05$ m are studied under laminar and turbulent regime operations, and plain design and added heat transfer structures.

It is demonstrated that cross-sectional plates are significantly better heat transfer enhancement structures compared.to reinforced bars.

In the laminar regime, the convective thermal resistance dominates the conductive, and is the limit factor for heat transfer. Therein, the addition of heat transfer structures does not improve the system performance, making it unsuitable for a regenerative thermal storage system.

In the turbulent regime, the conductive thermal resistance becomes the dominated factor. Therein, the addition of heat transfer structures lowers the conductive thermal resistance in one order of magnitude is found to be beneficial in terms of discharge efficiency, discharge

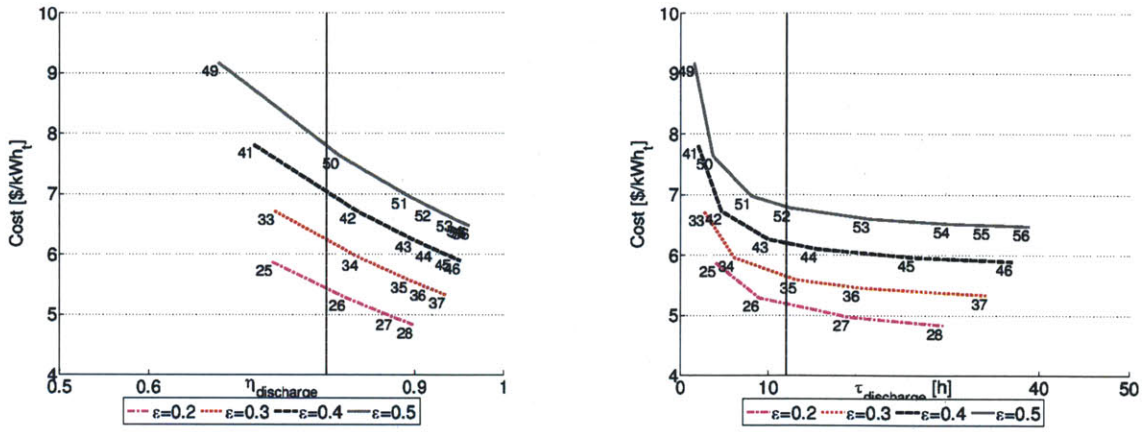

Figure 3-22: Storage cost [$/kWh$_t$] versus discharge efficiency (left) and discharge time (right) for the $b = 10\%$ plates added case studies at $Re_d = 10,000$ for $d = 0.1$ m

time, and storage cost.

Comparing with sensible solar salt thermal energy storage systems, like the two-tank type, or the CSPonD, significant reduction of solar salt has been obtained. However, the storage system still needs big quantities of HTF.

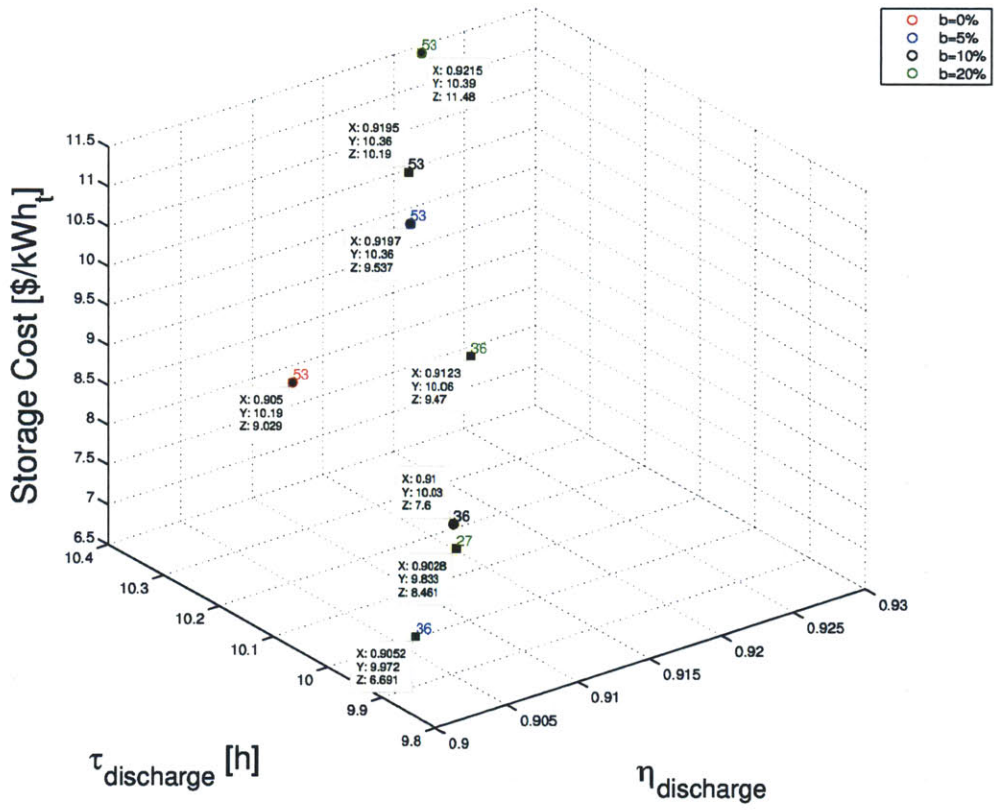

Figure 3-23: Storage configurations that satisfy a discharge time lower than 12 hours, and efficiency higher than 0.9. Storage cost $\bar{C}$ [$/kWh] is in the z axes, discharge time $\eta_{discharge}$ [h] is in the y axis, and discharge efficiency $\eta_{discharge}$ is in the y axes. Red circle corresponds for b = 0% aluminum, blue circles correspond for b = 5% aluminum, black circles correspond for b = 10% aluminum, and green circles correspond for b = 20% aluminum. Tube diameter d = 0.05 m for all of them.

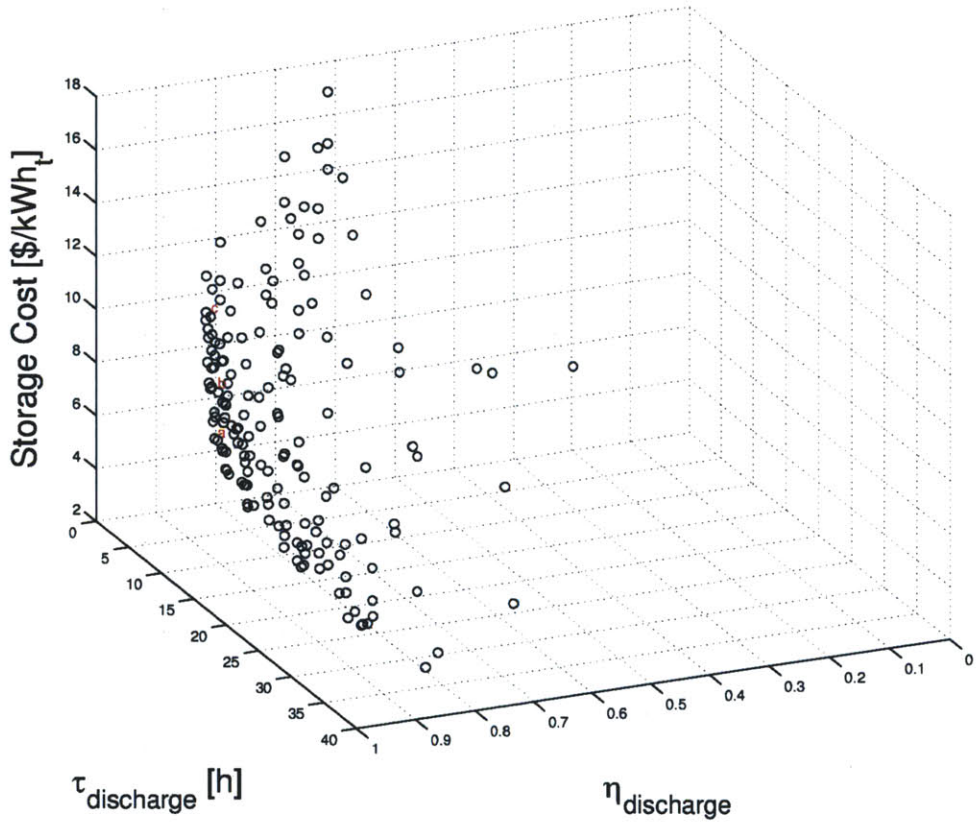

Figure 3-24: Pareto frontier for the total 448 case studies analyzed for $Re_d = 10,000$. Red circles in the figure correspond to the previous filtered configurations: the lowest $\bar{C}$ configuration (a), the lowest $\tau_{discharge}$ configuration (b), and the highest $\eta_{discharge}$ configuration (c).

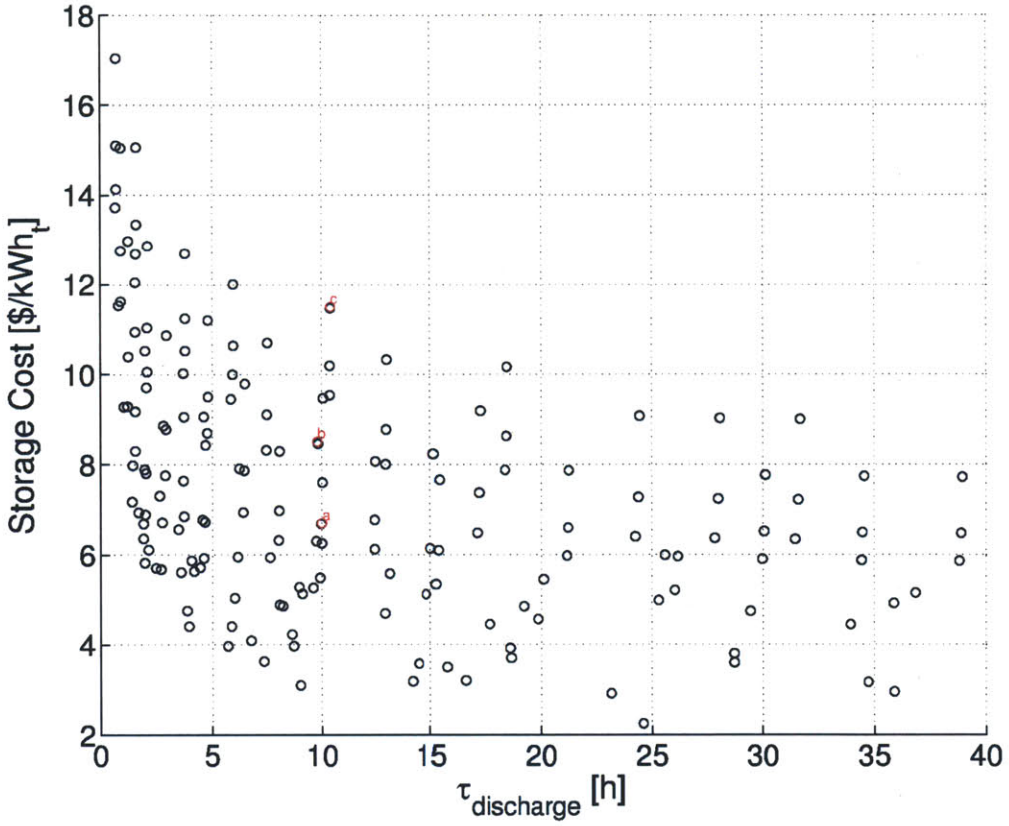

Figure 3-25: Pareto frontier for the total 448 case studies analyzed for Re_d = 10,000 represented in the projection plane $\bar{C} - \tau_{discharge}$. Red circles in the figure correspond to the previous filtered configurations: the lowest $\bar{C}$ configuration (a), the lowest $\tau_{discharge}$ configuration (b), and the highest $\eta_{discharge}$ configuration (c).

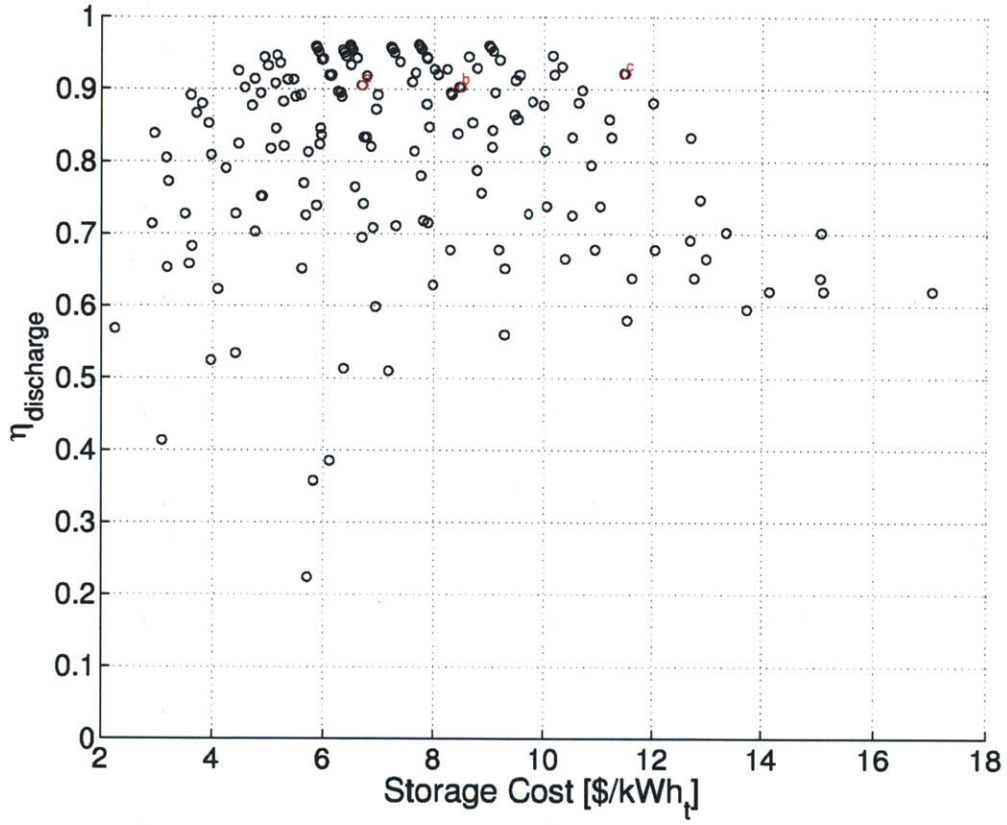

Figure 3-26: Pareto frontier for the total 448 case studies analyzed for Re_d = 10,000 represented in the projection plane $\eta_{discharge} - \bar{C}$. Red circles in the figure correspond to the previous filtered configurations: the lowest $\bar{C}$ configuration (a), the lowest $\tau_{discharge}$ configuration (b), and the highest $\eta_{discharge}$ configuration (c).

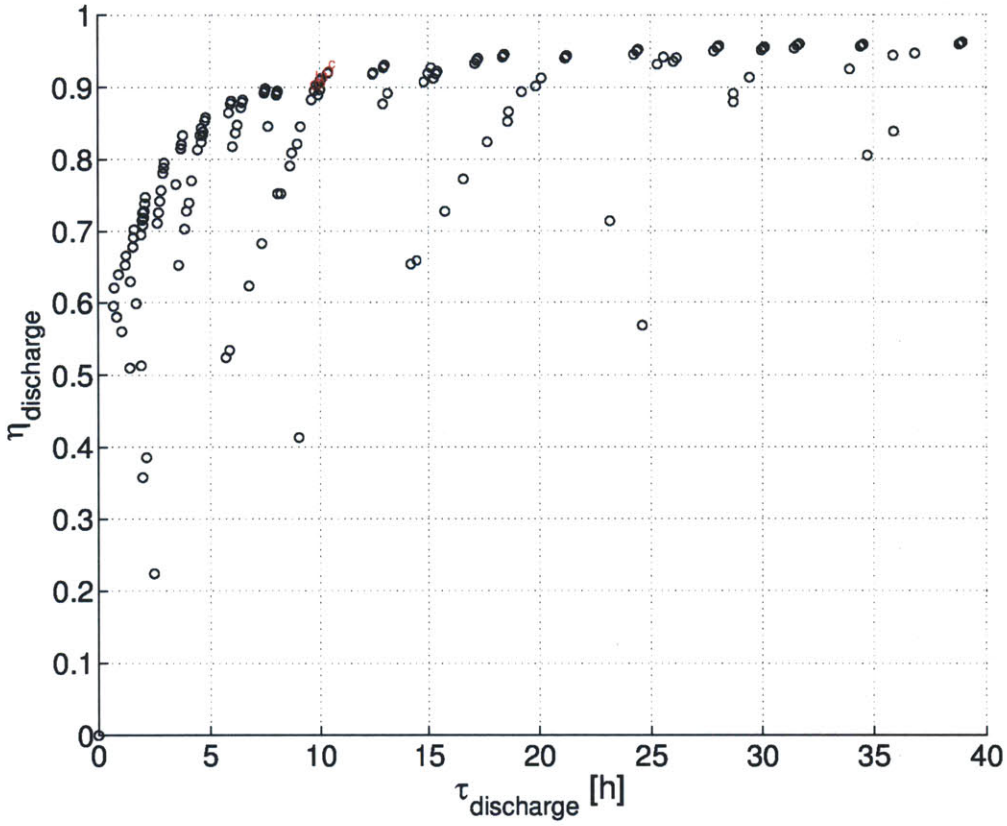

Figure 3-27: Pareto frontier for the total 448 case studies analyzed for Re_d = 10,000 represented in the projection plane $\eta_{discharge} - \tau_{discharge}$. Red circles in the figure correspond to the previous filtered configurations: the lowest $\bar{C}$ configuration (a), the lowest $\tau_{discharge}$ configuration (b), and the highest $\eta_{discharge}$ configuration (c).

THIS PAGE INTENTIONALLY LEFT BLANK

Nomenclature

Latin Letters

$\bar{C}$	Storage cost	[\$/kWh$_t$]
$\dot{m}$	Mass flow rate	[kg/s]
$\dot{Q}$	Heat transfer rate	[W]
$\dot{W}$	Power	[W]
$\hat{c}$	Time-weighted average electricity price	[\$/kWh]
A	Area	[m^2]
b	Volume percentage of heat transfer structure added	[%]
c	Electricity price	[\$/kWh]
c_p	Specific heat capacity	[J/(kg · K)]
$Cost$	Cost	[\$]
D	Storage block outer diameter	[m]
d	Storage block tube diameter	[m]
h	Convective heat transfer coefficient	[W/(m^2·K)]
L	Storage block length	[m]
N	Number of plates as heat transfer structure added	
Nu_d	Nusselt number based on the tube diameter d	
r	Cylindrical radial coordinate	[m]

R_h	Convective thermal resistance	[K/W]
R_r	Conductive thermal resistance in the radial direction	[K/W]
R_z	Conductive thermal resistance in the longitudinal direction	[K/W]
Re_d	Reynolds number based on the tube diameter d	
T	Temperature	[K]
t	Time	[s]
T_c	Coldest temperature of the thermal storage system	[K]
T_h	Highest temperature of the thermal storage system	[K]
U_{th}	Total thermal energy capacity	[kWh]
z	Cylindrical longitudinal coordinate	[m]
m	Mass	[kg]

CSP	Concentrated solar power	
CSPonD	Concentrated solar power on demand	
CTE	Coefficient of thermal expansion	[μm/m]
DAE	Differential algebraic equation	
HTF	Heat transfer fluid	
LCOE	Levelized cost of electricity	
NLP	Nonlinear programming	
PV	Photovoltaics	
RES	Renewable energy sources	

TES	Thermal energy storage
TOD	Time of day

Greek Letters

α	Thermal diffusivity	[m^2/s]
δ	Thickness	[m]
ϵ	Ratio of the tube cross sectional area to the total block cross sectional area	
η	Efficiency	
μ	Dynamic viscosity	[Pa·s]
ρ	Density	[kg/m^3]
τ	Time period	[s]
θ	Non-dimensional temperature	

Subscripts

$cold\,tank$	Cold salt tank
$field$	Collector field
$hot\,tank$	Hot salt tank
lid	Lid
off	Shutdown of the power block
on	Start-up of the power block
$power$	Power block
$aluminum$	Aluminum
$block$	Single storage block
$bulk$	Bulk fluid

charge	Charge process of the thermal energy storage system	
cold to hot	From the cold to the hot salt tank	
concrete	High temperature concrete	
cross	Cross section	
discharge	Discharge process of the thermal energy storage system	
hot to cold	From the hot to the cold salt tank	
HTF	Heat transfer fluid	
loss	Thermal losses of the thermal storage system	
metal	Metal	
output	Out of the thermal storage system into the power cycle	[MW]
plate	Plate shape	
purchased	Purchased from the grid	
return	Solar salt back to the cold salt tank from the power cycle heat exchanger	
s	Sunrise	
salt	Nitrate solar salt	
surface	Lateral surface	
pipe	Pipe material	
pump	Pumping of the HTF	

Bibliography

[1] M. A. Al-Nimr and M. A. Hader, *Transient conjugated heat transfer in developing laminar pipe flow*, Journal of Heat Transfer **116** (1994), no. 1, 234–236.

[2] J. M. Andujar, F. Rosa, and M. Geyer, *CESA-1 thermal storage system evaluation*, Solar Energy **46** (1991), no. 5, 305 – 312.

[3] L. T. Biegler, *Nonlinear programming: Concepts, algorithms, and applications to chemical processes*, MPS-SIAM Series on Optimization, SIAM-Society for Industrial and Applied Mathematics, 2010.

[4] A. Brooke, D. Kendrick, and A. Meeraus, *GAMS: A user's guide*, The Scientific Press, Redwood City, California, 1988.

[5] Coastal Chemical Company, *HITEC® heat transfer salt*, accessed May 2012.

[6] Coastal Chemical Company, *Hitec® solar salt*, accessed May 2012.

[7] R. M. Cotta, M. N. ziik, and D. S. McRae, *Transient heat transfer in channel flow with step change in inlet temperature*, Numerical Heat Transfer **9** (1986), no. 5, 619–630.

[8] F. Dinter, M. Geyer, and R. Tamme, *Thermal Energy Storage for Commercial Applications*, Springer-Verlag, 1991.

[9] A. S. Dorfman, *Conjugate Problems in Convective Heat Transfer*, CRC Press, 2010.

[10] I. A. Farhat and M. E. El-Hawary, *Optimization methods applied for solving the short-term hydrothermal coordination problem*, Electric Power Systems Research **79** (2009), no. 9, 1308 – 1320.

[11] FRIATEC, *Molten Salt Pump Curve*, 2009.

[12] H. W. Fricker, *Regenerative thermal storage in atmospheric air system solar power plants*, Energy **29** (2004), no. 56, 871 – 881.

[13] J. García-Barberena, P. Garcia, M. Sanchez, M. J. Blanco, C. Lasheras, A. Padrós, and J. Arraiza, *Analysis of the influence of operational strategies in plant performance using simulcet, simulation software for parabolic trough power plants*, Solar Energy **86** (2012), no. 1, 53 – 63.

[14] M. A. Geyer, *Thermal Storage for Solar Power Plants*, Solar Power Plants, C.-J. Winter, R. L. Sizmann, L. L. Vant-Hull, eds. Chap. 6, Springer-Verlag, New York, 1991.

[15] A. Ghobeity, E. Lizarraga-Garcia, and A. Mitsos, *Optimal Design and Operation of a volumetric Solar-Thermal Energy Receiver and Storage*, ECOS 2011, The 24th International Conference on Efficiency, Cost, Optimization, Simulation and Environmental Impact of Energy Systems, Novi Sad, Serbia, July 2011.

[16] A. Ghobeity, C. J. Noone, C. N. Papanicolas, and A. Mitsos, *Optimal Time-Invariant Operation of a Power and Water Cogeneration Solar-Thermal Plant*, Solar Energy **85** (2011), no. 9, 2295 – 2320.

[17] Amin Ghobeity and Alexander Mitsos, *Optimal Design and Operation of a Solar Energy Receiver and Storage*, Journal of Solar Energy Engineering **134** (2012), no. 3, 031005:1–9.

[18] A. Gil, M. Medrano, I. Martorell, A. Lazaro, P. Dolado, B. Zalba, and L. F. Cabeza, *State of the art on high temperature thermal energy storage for power generation. part 1-concepts, materials and modellization*, Renewable and Sustainable Energy Reviews **14** (2010), no. 1, 31 – 55 (English).

[19] S. M. Hasnain, *Review on sustainable thermal energy storage technologies, Part I: Heat storage materials and techniques*, Energy Conversion And Management **39** (1998), no. 11, 1127–1138.

[20] U. Herrmann and D.W. Kearney, *Survey of thermal energy storage for parabolic trough power plants*, Transactions of the ASME. Journal of Solar Energy Engineering **124** (2002), no. 2, 145 – 52.

[21] J. L. Hudson and S. G. Bankoff, *Asymptotic solutions for the unsteady graetz problem*, International Journal of Heat and Mass Transfer **7** (1964), no. 11, 1303 – 1307.

[22] Y.-Y. Jing, H. Bai, J.-J. Wang, and L. Liu, *Life cycle assessment of a solar combined cooling heating and power system in different operation strategies*, Applied Energy **92** (2012), no. 0, 843 – 853.

[23] D. Kearney, U. Herrmann, P. Nava, B. Kelly, R. Mahoney, J. Pacheco, R. Cable, N. Potrovitza, D. Blake, and H. Price, *Assessment of a molten salt heat transfer fluid in a parabolic trough solar field*, Journal of Solar Energy Engineering **125** (2003), no. 2, 170–176.

[24] D. Kearney, B. Kelly, U. Herrmann, R. Cable, J. Pacheco, R. Mahoney, H. Price, D. Blake, P. Nava, and N. Potrovitza, *Engineering aspects of a molten salt heat transfer fluid in a trough solar field*, Energy **29** (2004), no. 5-6, 861 – 870.

[25] D. Laing, C. Bahl, T. Bauer, M. Fiss, N. Breidenbach, and M. Hempel, *High-temperature solid-media thermal energy storage for solar thermal power plants*, Proceedings of the IEEE **100** (2012), no. 2, 516 –524.

[26] D. Laing, W.-D. Steinmann, M. Fiß, R. Tamme, T. Brand, and C. Bahl, *Solid media thermal storage development and analysis of modular storage operation concepts for parabolic trough power plants*, Journal of Solar Energy Engineering **130** (2008), no. 1, 011006.

[27] D. Laing, W.-D. Steinmann, R. Tamme, and C. Richter, *Solid media thermal storage for parabolic trough power plants*, Solar Energy **80** (2006), no. 10, 1283 – 1289.

[28] K.-T. Lee, , and W.-M. Yan, *Transient conjugated forced convection heat transfer with fully developed laminar flow in pipes*, Numerical Heat Transfer, Part A: Applications **23** (1993), no. 3, 341–359.

[29] P. Li, J. Van Lew, C. Chan, W. Karaki, J. Stephens, and J. E. O'Brien, *Similarity and generalized analysis of efficiencies of thermal energy storage systems*, Renewable Energy **39** (2012), no. 1, 388 – 402.

[30] T. F. Lin and J. C. Kuo, *Transient conjugated heat transfer in fully developed laminar pipe flows*, International Journal of Heat and Mass Transfer **31** (1988), no. 5, 1093 – 1102.

[31] M. Lively, *Wind energy: Too much of a good thing*, http://www.glgroup.com/News/Wind-Energy–Too-Much-of-a-Good-Thing-39717.html, accessed May 2012, 2009.

[32] MATLAB®, *version 7.11.0.584 (R2010b)*, The MathWorks Inc., Natick, Massachusetts, 2010.

[33] A. Mawire and M. McPherson, *Experimental characterisation of a thermal energy storage system using temperature and power controlled charging*, Renewable Energy **33** (2008), no. 4, 682 – 693.

[34] A. Mawire, M. McPherson, and R. R. J. van den Heetkamp, *Simulated energy and exergy analyses of the charging of an oilpebble bed thermal energy storage system for a solar cooker*, Solar Energy Materials and Solar Cells **92** (2008), no. 12, 1668 – 1676.

[35] A. Mawire, M. McPherson, and R. R. J. van den Heetkamp, *Thermal performance of a small oil-in-glass tube thermal energy storage system during charging*, Energy **34** (2009), no. 7, 838 – 849.

[36] A. Mawire, M. McPherson, R. R. J. van den Heetkamp, and S. J. P. Mlatho, *Simulated performance of storage materials for pebble bed thermal energy storage (tes) systems*, Applied Energy **86** (2009), no. 78, 1246 – 1252.

[37] A. Mawire, M. McPherson, R. R. J. van den Heetkamp, and S. H. Taole, *Experimental volumetric heat transfer characteristics between oil and glass pebbles in a small glass tube storage*, Energy **35** (2010), no. 3, 1256 – 1263.

[38] A. F. Mills and V. Ganesan, *Heat Transfer*, Pearson, 1999.

[39] COMSOL Multiphysics® 4.2a, *http://www.comsol.com/*, 2012.

[40] Y. S. Muzychka, E. Walsh, and P. Walsh, *Simple models for laminar thermally developing slug flow in noncircular ducts and channels*, Journal of Heat Transfer **132** (2010), no. 11, 111702.

[41] M. Nicolosi, *Wind power integration and power system flexibility-an empirical analysis of extreme events in Germany under the new negative price regime*, Energy Policy **38** (2010), no. 11, 7257 – 7268.

[42] B. Norton, *Solar Energy Thermal Technology*, Springer-Verlag, 1992.

[43] NREL, *Solar Advisor Model® 4.12*, 2010.

[44] JACOBIAN Modeling Numerica Technology and Optimization Software, *http://www.numericatech.com*, 2009.

[45] S. Olek, E. Elias, E. Wacholder, and S. Kaizerman, *Unsteady conjugated heat transfer in laminar pipe flow*, International Journal of Heat and Mass Transfer **34** (1991), no. 6, 1443 – 1450.

[46] Operador del Mercado Ibérico, Polo Español, *Hourly Electricity Price*, http://www.omie.es/inicio, 2012.

[47] J. I. Ortega, J. I. Burgaleta, and F. M. Téllez, *Central receiver system solar power plant using molten salt as heat transfer fluid*, Journal of Solar Energy Engineering **130** (2008), no. 2, 024501.

[48] J. E. Pacheco, S. K. Showalter, and W. J. Kolb, *Development of a Molten-Salt Thermocline Thermal Storage System for Parabolic Trough Plants*, Journal of Solar Energy Engineering **124** (2002), no. 2, 153–159.

[49] N. P. Padhy, *Unit commitment-a bibliographical survey*, Power Systems, IEEE Transactions on **19** (2004), no. 2, 1196 – 1205.

[50] M. Perlmutter and R. Siegel, *Unsteady laminar flow in a duct with unsteady heat addition*, Journal of Heat Transfer **83** (1961), no. 4, 432–440.

[51] B. Prior, *Cost and lcoe by generation technology, 2009-2020*, http://www.greentechmedia.com/images/wysiwyg/research-blogs/GTM-LCOE-Analysis.pdf, accessed May 2012, 2011.

[52] Public Utility Commission of Texas, *http://www.puc.state.tx.us/wmo/index.cfm?tab=1*, accessed May 2011.

[53] N. Rafidi and W. Blasiak, *Thermal performance analysis on a two composite material honeycomb heat regenerators used for hitac burners*, Applied Thermal Engineering **25** (2005), no. 1718, 2966 – 2982.

[54] Red Eléctrica de España, *Hourly Electricity Demand*, http://www.ree.es/ingles/home.asp, 2012.

[55] A. Rovira, M. J. Montes, M. Valdes, and J. M. Martínez-Val, *Energy management in solar thermal power plants with double thermal storage system and subdivided solar field*, Applied Energy **88** (2011), no. 11, 4055 – 4066.

[56] D. J. Schutte, M. M. Rahman, and A. Faghri, *Transient conjugate heat transfer in a thick-walled pipe with developing laminar flow*, Numerical Heat Transfer, Part A: Applications **21** (1992), no. 2, 163–186.

[57] R. Paneer Selvam and M. Hale, *Development and Performance Evaluation of High Temperature Concrete for Thermal Energy Storage for Solar Power Generation*, accessed May 2012, 2011.

[58] R. Panneer Selvam and M. Castro, *3D FEM Model to Improve the Heat Transfer in Concrete for Thermal Energy Storage in Solar Power Generation*, ASME Conference Proceedings (2010), no. 43956, 699–707.

[59] R. Siegel and M. Perlmutter, *Laminar heat transfer in a channel with unsteady flow and wall heating varying with position and time*, Journal of Heat Transfer **85** (1963), no. 4, 358–365.

[60] A. Slocum, J. Buongiorno, C. Forsberg, T. McKrell, A. Mitsos, J. C. Nave, D. Codd, A. Ghobeity, C. Noone, S. Passerini, F. Rojas, and J. Rees, *Concentrated solar power on demand*, Solar Energy **85** (2011), 1519 – 1529.

[61] E. M. Sparrow and F. N. De Farias, *Unsteady heat transfer in ducts with time-varying inlet temperature and participating walls*, International Journal of Heat and Mass Transfer **11** (1968), no. 5, 837 – 853.

[62] J. Sucec, *An improved quasi-steady approach for transient conjugated forced convection problems*, International Journal of Heat and Mass Transfer **24** (1981), no. 10, 1711 – 1722.

[63] J. Sucec, *Exact solution for unsteady conjugated heat transfer in the thermal entrance region of a duct*, Journal of Heat Transfer **109** (1987), no. 2, 295–299.

[64] J. Sucec, *Unsteady conjugated forced convective heat transfer in a duct with convection from the ambient*, International Journal of Heat and Mass Transfer **30** (1987), no. 9, 1963 – 1970.

[65] J. Sucec, *Unsteady forced convection with sinusoidal duct wall generation: the conjugate heat transfer problem*, International Journal of Heat and Mass Transfer **45** (2002), no. 8, 1631 – 1642.

[66] J. Sucec and A. M. Sawant, *Unsteady, conjugated, forced convection heat transfer in a parallel plate duct*, International Journal of Heat and Mass Transfer **27** (1984), no. 1, 95 – 101.

[67] R. Tamme, D. Laing, and W.-D. Steinmann, *Advanced thermal energy storage technology for parabolic trough*, Journal of Solar Energy Engineering **126** (2004), no. 2, 794–800.

[68] J. S. Travelho and W. F. N. Santos, *Unsteady conjugate heat transfer in a circular duct with convection from the ambient and periodically varying inlet temperature*, Journal of Heat Transfer **120** (1998), no. 2, 506–510.

[69] T. M. Tveit, T. Savola, and C. J. Fogelholm, *Modelling of steam turbines for mixed integer nonlinear programming (minlp) in design and off-design conditions of chp plants*, Proceedings of the 46th Conference on Simulation and Modeling (SIMS 2005) (Trondheim, Norway), Trondheim, Tapor Academic Press, 13-14 October 2005, pp. 335–344.

[70] Tyco Thermal Controls, *http://www.tycothermal.com/*, accessed March 2012.

[71] C. E. Tyner, J. P. Sutherland, and W. R. J. Gould, *Solar Two: A Molten Salt Power Tower Demonstration*, Tech. report, Sandia National Laboratories, Albuquerque, NM, 1995.

[72] A. Wächter and L. T. Biegler, *On the implementation of an interior-point filter line-search algorithm for large-scale nonlinear programming*, Mathematical Programming **106** (2006), 25 – 57.

[73] K.Y. Wang, F. Kreith, R.E. West, and P. Lynn, *High temperature sensible heat storage options*, Solar Energy (1985), 198 – 205.

[74] M. Wittmann, M. Eck, R. Pitz-Paal, and H. Müller-Steinhagen, *Methodology for optimized operation strategies of solar thermal power plants with integrated heat storage*, Solar Energy **85** (2011), no. 4, 653 – 659.

[75] H. Y. Yamin, *Review on methods of generation scheduling in electric power systems*, Electric Power Systems Research **69** (2004), no. 23, 227 – 248.

[76] W.-M. Yan, *Transient conjugated heat transfer in channel flows with convection from the ambient*, International Journal of Heat and Mass Transfer **36** (1993), no. 5, 1295 – 1301.

[77] W.-M. Yan, *Unsteady conjugated heat transfer in turbulent channel flows with convection from the ambient*, International Journal of Heat and Mass Transfer **38** (1995), no. 11, 2101 – 2108.

[78] W.-M. Yan, Y. L. Tsay, and T. F. Lin, *Transient conjugated heat transfer in laminar pipe flows*, International Journal of Heat and Mass Transfer **32** (1989), no. 4, 775 – 777.

[79] Z. Yang and S. V. Garimella, *Thermal analysis of solar thermal energy storage in a molten-salt thermocline*, Solar Energy **84** (2010), no. 6, 974 – 985.